https://dx.doi.org/10.1016/j.measurement.2023.112967

Discrete integration for measuring aerodynamic loads on trains in crosswinds − realizable strategies of discretization and discrete integration

Hongrui Gao [a, b, c, d], Tanghong Liu [a, c, d, *], Zhiqi Liu [a, c, d], Xiaoshuai Huo [a, c, d], Jie Zhang [a, c, d], Xinran Wang [a, c, d], Zhengwei Chen [e]

[a] Key Laboratory of Traffic Safety on Track, Ministry of Education, School of Traffic & Transportation Engineering, Central South University, Changsha 410075, China

[b] Department of Mechanical Engineering, National University of Singapore, Singapore 117575, Singapore

[c] Joint International Research Laboratory of Key Technology for Rail Traffic Safety, School of Traffic & Transportation Engineering, Central South University, Changsha 410075, China

[d] National & Local Joint Engineering Research Center of Safety Technology for Rail Vehicle, School of Traffic & Transportation Engineering, Central South University, Changsha 410075, China

[e] Department of Civil and Environmental Engineering, The Hong Kong Polytechnic University, Hong Kong 999077, China

Abstract

Discrete integration occupies an important place in train aerodynamic tests in crosswinds. Improved delayed detached eddy simulations based on shear stress transport k-ω turbulence models were carried out to calculate the side force, lift, rolling moment around the lee rail, and surface pressure on bluff and streamlined vehicles. The changepoints and piecewise linearities of the pressure coefficients were evaluated, and the maximum coefficient of determination in the elements was 0.9973. A realizable strategy of the discretization based on the Lagrange rectangular elements was suggested, including the largest lengths and numbers of the elements. From this, a strategy of the discrete integration was presented to measure the aerodynamic loads, considering the real orientation of the elements. The maximum errors of the mean aerodynamic load coefficients of the bluff and streamlined vehicles were 4.1% and 2.2% (except the mean lift coefficient of the bluff vehicle), respectively. The errors were less than those in the previous studies, especially for the streamlined vehicle, which reduced by up to 8.7%. The unsteady aerodynamic loads with no delay obtained by the strategies were near to natural ones in the frequency range that people would be concerned about in crosswinds (at the Strouhal number

* Corresponding author. Key Laboratory of Traffic Safety on Track, Ministry of Education, School of Traffic & Transportation Engineering, Central South University, Changsha, 410075, China.
E-mail address: lth@csu.edu.cn (T. Liu).

of less than 0.4). Some suggestions were made for using the strategies in the full-scale tests and model tests, which provided a foundation for further studies of the running safety in natural crosswinds.

Keywords

Crosswinds, Surface pressure distributions, Aerodynamic load coefficients, Lagrange rectangular elements, Discretization, Discrete integration

1. Introduction

There is a marked increase in aerodynamic loads on trains in crosswinds, threatening people's life, property, and the running safety of the trains [1]. The aerodynamic loads on the trains in crosswinds have been studied by numerical simulations [2–10], model tests [11–15], and full-scale tests [16–20] to improve their running safety.

The numerical simulations, model tests, and full-scale tests are the basic means of this issue [21–23]. The numerical simulations have developed rapidly in recent years, which can capture the details associated with the flow around the train [9,13], such as the pressure, velocity, vortex, and turbulence. Unfortunately their results need to be validated by the model tests and full-scale tests [17,24]. Such techniques can obtain the accurate aerodynamic loads and lay emphasis on different aspects. The model tests have the advantages of low cost and easy control and implementation [25–27], and apply to the base research under the ideal conditions such as the uniform onset flow and atmospheric boundary layer. The Reynolds' numbers in the full-scale tests are much larger than those in the model tests [28,29], and the full-scale tests can obtain the unsteady aerodynamic loads on the trains in natural crosswinds [18,30]. They apply to the specific research on the aerodynamic loads and running safety of the trains and can help to improve the numerical simulations and model tests. The model tests and full-scale tests can be carried out on the static and moving trains with different methods.

For the static trains, the aerodynamic loads were measured using external force balances [13,31–35] and internal force balances [26,27,30,36–41] in the model tests. Sanquer et al. [24] developed a new method (named discrete integration) based on pressure measurements to know the aerodynamic loads in the wind tunnel tests (static model tests), where the loads were measured with the pressure integration at 300 pressure taps on the vehicle. It provided a reliable way to access the aerodynamic loads when the taps are dense enough. The proposed method allowed the rolling moment with small uncertainty and global understanding of the aerodynamic loads, which was useful for the dynamic behaviour simulations. Such method has been used in some wind tunnel tests [11,42–44], whose numbers of the taps in the tests are listed

in The number and layout of the taps in the tests in **Error! Not a valid bookmark self-reference.** were not the same. At present how to determine the number of the pressure taps is always a real problem. Liu et al. [48] obtained a reasonable layout of the taps on the streamlined high-speed train at the yaw angles of 5.87−90°, where the head, middle, and tail car were equipped with 240, 224, and 240 taps, respectively. However, such number of the taps is hard to achieve with space limitation in the tests, especially in the full-scale tests. Most numbers of the taps in the tests in Table 1 were far less than that in Liu et al. [48], nevertheless, their results were still accurate. The improve related to increasing the number of the taps is small considering the uncertainty, as Dorigatti et al. [25] mentioned, when the taps achieve the target number. Therefore, it is necessary to study a realizable layout of the taps on the train in crosswinds taking account of various circumstances.

In this work, the aerodynamic loads and surface pressure on the bluff and streamlined vehicle in crosswinds were calculated by the numerical simulations. From this, realizable strategies of discretization and discrete integration for aerodynamic load measurements were suggested, where the Lagrange rectangular elements were used for the discretization of the vehicle surfaces, and that the aerodynamic loads were calculated by the discrete integration with the correction of the real orientation. The reappearance of the mean and unsteady aerodynamic loads was evaluated. The strategies would help the model tests and full-scale tests based on the discrete integration. The integration strategy associated with the Lagrange rectangular elements is presented in Section 2. The details and validation of the numerical simulations are reported in Section 3. Section 4 studies the discretization strategy of the bluff and streamlined vehicle and checks the accuracy of the strategy from a mean and unsteady standpoint. Some brief conclusions are described in Section 5.

Table 1. The aerodynamic load measurements were made on the static trains using the load cells in the full-scale tests [16,19].

For the moving trains, the aerodynamic loads were measured still using the force balance [12,45] and load cells [46] in the model tests, between which there was no essential difference. However, the mechanical noise interference caused by the track-induced vibrations reportedly affected the accuracy of the aerodynamic loads [12,46]. Dorigatti et al. [25] calculated the aerodynamic loads by discrete integration of the pressure at 110 taps in the moving model tests to mitigate the issues with the mechanical noise above-mentioned. There were still a few moving model tests calculating the aerodynamic loads on both the bluff and streamlined vehicles by discrete integration [17,47], whose numbers of the taps are listed in The number and layout of the taps in the tests in **Error! Not a valid bookmark self-reference.** were not the same. At present how to determine the number of the pressure taps is always a real problem.

Liu et al. [48] obtained a reasonable layout of the taps on the streamlined high-speed train at the yaw angles of 5.87−90°, where the head, middle, and tail car were equipped with 240, 224, and 240 taps, respectively. However, such number of the taps is hard to achieve with space limitation in the tests, especially in the full-scale tests. Most numbers of the taps in the tests in **Error! Not a valid bookmark self-reference.** were far less than that in Liu et al. [48], nevertheless, their results were still accurate. The improve related to increasing the number of the taps is small considering the uncertainty, as Dorigatti et al. [25] mentioned, when the taps achieve the target number. Therefore, it is necessary to study a realizable layout of the taps on the train in crosswinds taking account of various circumstances.

In this work, the aerodynamic loads and surface pressure on the bluff and streamlined vehicle in crosswinds were calculated by the numerical simulations. From this, realizable strategies of discretization and discrete integration for aerodynamic load measurements were suggested, where the Lagrange rectangular elements were used for the discretization of the vehicle surfaces, and that the aerodynamic loads were calculated by the discrete integration with the correction of the real orientation. The reappearance of the mean and unsteady aerodynamic loads was evaluated. The strategies would help the model tests and full-scale tests based on the discrete integration. The integration strategy associated with the Lagrange rectangular elements is presented in Section 2. The details and validation of the numerical simulations are reported in Section 3. Section 4 studies the discretization strategy of the bluff and streamlined vehicle and checks the accuracy of the strategy from a mean and unsteady standpoint. Some brief conclusions are described in Section 5.

Table 1. Similarly, at the present period, the aerodynamic loads on the moving trains were calculated indirectly by the discrete integration of the pressure in the full-scale tests [17,18,20], as listed in The number and layout of the taps in the tests in **Error! Not a valid bookmark self-reference.** were not the same. At present how to determine the number of the pressure taps is always a real problem. Liu et al. [48] obtained a reasonable layout of the taps on the streamlined high-speed train at the yaw angles of 5.87−90°, where the head, middle, and tail car were equipped with 240, 224, and 240 taps, respectively. However, such number of the taps is hard to achieve with space limitation in the tests, especially in the full-scale tests. Most numbers of the taps in the tests in **Error! Not a valid bookmark self-reference.** were far less than that in Liu et al. [48], nevertheless, their results were still accurate. The improve related to increasing the number of the taps is small considering the uncertainty, as Dorigatti et al. [25] mentioned, when the taps achieve the target number. Therefore, it is necessary to study a realizable layout of the taps on the train in crosswinds taking account of various circumstances.

In this work, the aerodynamic loads and surface pressure on the bluff and streamlined vehicle in crosswinds were calculated by the numerical simulations. From this, realizable strategies of discretization and discrete integration for aerodynamic load measurements were suggested, where the Lagrange rectangular elements were used for the discretization of the vehicle surfaces, and that the aerodynamic loads were calculated by the discrete integration with the correction of the real orientation. The reappearance of the mean and unsteady aerodynamic loads was evaluated. The strategies would help the model tests and full-scale tests based on the discrete integration. The integration strategy associated with the Lagrange rectangular elements is presented in Section 2. The details and validation of the numerical simulations are reported in Section 3. Section 4 studies the discretization strategy of the bluff and streamlined vehicle and checks the accuracy of the strategy from a mean and unsteady standpoint. Some brief conclusions are described in Section 5.

Table 1, rather than measured directly [48].

The number and layout of the taps in the tests in **Error! Not a valid bookmark self-reference.** were not the same. At present how to determine the number of the pressure taps is always a real problem. Liu et al. [48] obtained a reasonable layout of the taps on the streamlined high-speed train at the yaw angles of 5.87−90°, where the head, middle, and tail car were equipped with 240, 224, and 240 taps, respectively. However, such number of the taps is hard to achieve with space limitation in the tests, especially in the full-scale tests. Most numbers of the taps in the tests in **Error! Not a valid bookmark self-reference.** were far less than that in Liu et al. [48], nevertheless, their results were still accurate. The improve related to increasing the number of the taps is small considering the uncertainty, as Dorigatti et al. [25] mentioned, when the taps achieve the target number. Therefore, it is necessary to study a realizable layout of the taps on the train in crosswinds taking account of various circumstances.

In this work, the aerodynamic loads and surface pressure on the bluff and streamlined vehicle in crosswinds were calculated by the numerical simulations. From this, realizable strategies of discretization and discrete integration for aerodynamic load measurements were suggested, where the Lagrange rectangular elements were used for the discretization of the vehicle surfaces, and that the aerodynamic loads were calculated by the discrete integration with the correction of the real orientation. The reappearance of the mean and unsteady aerodynamic loads was evaluated. The strategies would help the model tests and full-scale tests based on the discrete integration. The integration strategy associated with the Lagrange rectangular elements is presented in Section 2. The details and validation of the numerical simulations are reported in Section 3. Section 4 studies the discretization strategy of the bluff

and streamlined vehicle and checks the accuracy of the strategy from a mean and unsteady standpoint. Some brief conclusions are described in Section 5.

Table 1 Discrete integration of pressure in previous model tests and full-scale tests.

Means	References	Numbers of taps	Aerodynamic loads
Wind tunnel tests	Gallagher et al. [17]	313	Side force and lift
	Sanquer et al. [24]	300	Side force, lift, and rolling moment
	Dorigatti et al. [25]	164	Side force, lift, and rolling moment
	Hashmi et al. [43]	162	Side force, lift, and rolling moment
	Baker and Sterling [11]	Approximately 100	Side force and lift
	Avila-Sanchez et al. [42]	48	Side force, lift, and rolling moment
	He et al. [44]	18 for train-head section and 17 for train-body section	Side force, lift, and rolling moment of sections
Moving model tests	Dorigatti et al. [25]	110	Side force, lift, and rolling moment
	Soper et al. [47]	75 for loading efficiency of 100% and 53 for that of 66%	Side force, lift, and rolling moment
	Gallagher et al. [17]	17	Side force per unit length
Full-scale tests	Gao et al. [18]	106 (58 taps on windward and leeward side and 48 taps on bottom and roof)	Side force, lift, and rolling moment
	Liu et al. [20]	100 (58 taps on windward and leeward side and 42 taps on bottom and roof)	Side force, lift, and rolling moment
	Gallagher et al. [17]	17	Side force per unit length

2. Measuring methodology

2.1. Discrete integration

The aerodynamic loads of the vehicles in crosswinds include the pressure and viscous loads. The viscous ones account for only a small share of the aerodynamic loads, which are dominated by the pressure ones. Liu et al. [48] showed that the pressure side force and lift were larger than 96% of the total forces at the yaw angles of 5.87−30°. Therefore, the pressure loads are sufficient to cover the aerodynamic loads in crosswinds, which can be obtained by the discrete integration of the pressure [24,42].

The aerodynamic loads of the test vehicles can be calculated by the discrete integral of the pressure over the vehicles, which is an indirect measurement method [18]. The vehicle surfaces are discretized using a series of elements, on which the aerodynamic loads are calculated by the integration. The aerodynamic loads on the vehicles are the sums of those on all the elements [48].

The purpose of the discrete integration is to obtain the aerodynamic loads of the test vehicles through those on each element, as mentioned above, rather than the continuously changed pressure on the vehicle surface. The discrete integration would be used in full-scale tests and model tests with the simplest possible elements. Under such demand, the elements should be simple, containing the pressure at the nodes, but not the rate of the pressure change. Therefore, combining with the shape of the vehicle, the Lagrange rectangular elements were used, instead of the triangular elements, Hermite rectangular elements, or Serendipity elements.

A Lagrange rectangular element discretizing the vehicle surfaces is shown in Fig. 1, which includes the nodes A, B, C, and D as well as the midpoint M of the element. Xiong et al. [49] discretized the vehicle surface using such elements.

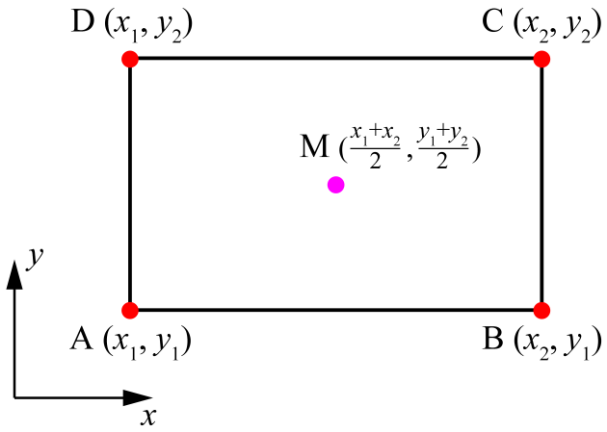

Fig. 1. Lagrange rectangular element.

The aerodynamic force F_e on the element is

$$F_e = \iint_D p dx dy = p_M S_e \tag{1}$$

where p_M is the pressure at the midpoint M, and S_e is the area of the element.

The pressure at the midpoint and the area of the element can be used to calculate the aerodynamic forces on the element. Hence the aerodynamic forces of the test vehicles can be obtained by measuring the pressure at the midpoints of the elements on the vehicle surfaces, consistent with the previous studies [17,18,20,25,43,47]. The side force of the vehicles is the vectorial sum of the aerodynamic forces on the elements on the windward and leeward sides, and the lift is the vectorial sum of those on the elements on the bottom and roof.

The rolling moment on the Lagrange rectangular element cannot be obtained only from

the pressure at the midpoint of the element, unlike the aerodynamic forces, but also the pressure at the nodes. However, it is a different story for the rolling moment on the adjacent elements, as shown in Fig. 2.

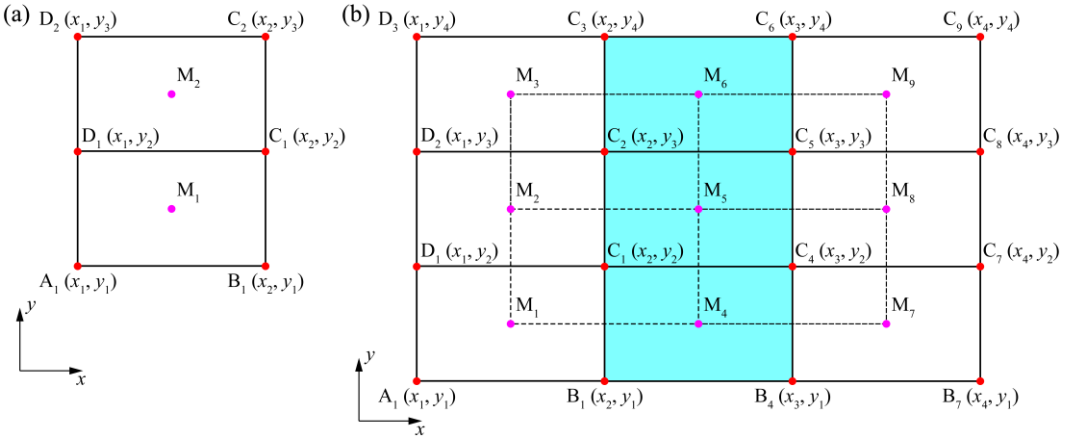

Fig. 2. Adjacent Lagrange rectangular elements: (a) adjacent two elements and (b) adjacent three elements.

Fig. 2(a) shows the two adjacent Lagrange rectangular elements, where y of the element $A_1B_1C_1D_1$ varies between y_1 and y_2 and that of the element $D_1C_1C_2D_2$ ranges from y_2 to y_3. The total rolling moment on the two adjacent elements, as a function of the pressure at the midpoint and their sizes, is calculated by

$$M_{xe1} + M_{xe2} = p_{M1} S_e \frac{2y_1 + y_2}{3} + p_{M2} S_e \frac{y_2 + 2y_3}{3} \tag{2}$$

where M_{xe1} and M_{xe2} are the rolling moments on the elements $A_1B_1C_1D_1$ and $D_1C_1C_2D_2$ in Fig. 2(a), respectively, and p_{M1} and p_{M2} are the pressures at the midpoints M1 and M2, respectively.

Fig. 2(b) shows the three adjacent Lagrange rectangular elements, which are the three light cyan elements ($B_1B_4C_4C_1$, $C_1C_4C_5C_2$, and $C_2C_5C_6C_3$) in the figure. Their y ranges are y_1–y_2, y_2–y_3, and y_3–y_4, respectively. The other elements are used to calculate the total rolling moment on the three adjacent elements by

$$M_{xe4} + M_{xe5} + M_{xe6} = \left(M_{xe4} + M_{xe5}\right) + \left(M_{xe5} + M_{xe6}\right) - M_{xe5} \tag{3}$$

$$M_{xe5} = \frac{1}{4} S_e \left(p_{C1} \frac{2y_2 + y_3}{3} + p_{C4} \frac{2y_2 + y_3}{3} + p_{C5} \frac{y_2 + 2y_3}{3} + p_{C2} \frac{y_2 + 2y_3}{3} \right) \tag{4}$$

where M_{xe4}, M_{xe5}, and M_{xe6} are the rolling moments on the elements $B_1B_4C_4C_1$, $C_1C_4C_5C_2$, and $C_2C_5C_6C_3$ in Fig. 2(b), respectively, and p_{C1}, p_{C4}, p_{C5}, and p_{C2} are the pressures at the nodes C_1, C_4, C_5, and C_2, respectively.

However, the pressures at the nodes C_1, C_4, C_5, and C_2 cannot be provided directly. The elements $M_1M_4M_5M_2$, $M_4M_7M_8M_5$, $M_5M_8M_9M_6$, and $M_2M_5M_6M_3$ in Fig. 2(b) are approximated the Lagrange rectangular elements because the surface pressure changes continuously and slowly. Hence the pressure at the point C_1 can be calculated in those at the

points M_1, M_4, M_5, and M_2. The same is true of the pressure at the points C_4, C_5, and C_2. It is worth noting that there are still errors with the less common measurement of the total rolling moment on the three adjacent elements. The proposed algorithm can decrease the error (see Section 4.3) compared with the measurements in the previous studies, where the aerodynamic forces on the elements and their arms were used to calculate the rolling moment on the elements.

2.2. Correction in real orientation of elements

The pressures should be projected into the directions of the aerodynamic forces since they are in the directions of the element normal. Supposing the normal vector to the midpoint M of the element is $\vec{n} = \left(n_x, n_y, n_z\right)$, the projection is

$$p_{\mathrm{M}y} = \frac{n_y}{|\vec{n}|} p_{\mathrm{M}} \tag{5}$$

$$p_{\mathrm{M}z} = \frac{n_z}{|\vec{n}|} p_{\mathrm{M}} \tag{6}$$

where p_{My} and p_{Mz} are the projections of p_{M} to the directions of y- and z-axis, which are specially formulated for the side force and lift, respectively.

Only the real orientations of the midpoints − rather than those of all the points on the elements − are considered, which interfere with the truth. It is difficult to address the real orientations of all the points, which is the same as the truth. Nevertheless, such correction in the real orientation of the elements still helps the aerodynamic loads.

2.3. Pressure and aerodynamic load coefficients

According to the standard EN 14067−1 [50], the pressure and aerodynamic load coefficients are defined as

$$C_p = \frac{p - p_0}{q} \tag{7}$$

$$C_{Fy} = \frac{F_y}{qS} \tag{8}$$

$$C_{Fz} = \frac{F_z}{qS} \tag{9}$$

$$C_{Mx,\,\mathrm{lee}} = \frac{M_{x,\,\mathrm{lee}}}{qSH} \tag{10}$$

where C_p is the pressure coefficient, p is the pressure, p_0 is the reference static pressure, which was obtained upstream of the models where the pressure was not affected by the models, q is the dynamic pressure, C_{Fy}, C_{Fz}, and $C_{Mx,\,\mathrm{lee}}$ are the side force coefficient, lift coefficient, and rolling moment coefficient around the lee rail, respectively, F_y, F_z, and $M_{x,\,\mathrm{lee}}$ are the side force, lift, and rolling moment around the lee rail, respectively, S is the characteristic area, i.e., the cross-sectional area, and H is the height of the test vehicles.

2.4. Experimental uncertainty

The uncertainties of the pressure and aerodynamic load coefficients are influenced by the individual uncertainty associated with the pressure and velocity. The calculation formulas have been presented in our previous work [18]. The errors in Section 4.3 could be used to calculate the type-B uncertainties of the aerodynamic load coefficients and then their combined standard uncertainties.

3. Wind tunnel tests and numerical simulations

3.1. Wind tunnel tests and train models

The aerodynamic characteristics of bluff trains and streamlined trains are different in crosswinds. The strategies of discretization on their surface were studied.

For a bluff train, wind tunnel tests were carried out in a drawing wind tunnel at China Aerodynamics Research and Development Center in Gao et al. [51]. The cross-section of the test section is 8 m × 6 m. The wind speed range is 20–100 m/s. The turbulence level is 0.1%, and the flow deflection angle is less than 0.5°. The boundary layer techniques were used in the wind tunnel, including a boundary layer suction and a splitter plate. 1:15 models of the bluff train and ground (the embankment and rails) were installed on the plate, as shown in Fig. 3(a). No blockage correction was needed for the blockage ratio was smaller than 5%. Gao et al. [51] illustrated the experimental setup, all of which satisfied the standard EN 14067−6 [52].

For a streamlined train, wind tunnel tests were carried out in the high-speed test section (3 m × 3 m) of the Wind Tunnel Laboratory of Central South University. The wind tunnel is a circulating wind tunnel with slotted walls. The wind speed range is 0–94 m/s. The turbulence level is less than 0.5%, and the unevenness of the velocity is less than 1%, as well as the flow deflection angle is less than 1°. 1:20 models of the streamlined train and ground (the subgrade and rails) were installed on the splitter plate, whose upstream end was rounded, as shown in Fig. 3(b). The blockage correction was used for the blockage ratio (the ratio of the projected side area of the total modelled configuration to the wind tunnel cross-sectional area) was 9.1%, between 5% and 15%. The experimental setup, boundary layer, and blockage correction were

the same as our previous work [30] and satisfied the standard EN 14067−6 [52].

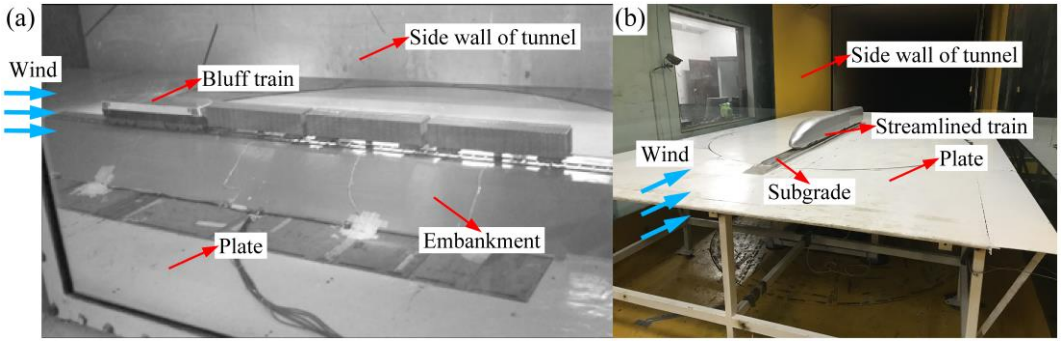

Fig. 3. Wind tunnel tests: (a) bluff train [51] and (b) streamlined train.

The yaw angle of 30°, which is the angle between the train axis and wind tunnel axis, is considered at the top of the realistic range for high-speed trains because the ratio of the wind speed to the train speed is low [26,39,43]. Hence the bluff train and streamlined train were measured at the yaw angle of 30° for unity. It is worth noting that the yaw angles shown in Fig. 3 are not 30°, but other angles from the same wind tunnel tests.

The train models and ground configurations in the wind tunnel tests and numerical simulations are the same. Fig. 4(a) and (b) show the bluff train model and ground configuration. The train model was formed from a locomotive and three freight wagons, and the second freight wagon was the test model (denoted as BTV). BTV was tested using a freight wagon model as upstream body. The ratio of the total length of the train model to the width of the tunnel was less than 0.75. The height of the embankment was 1.23H, and the slope was 2/3. Gao et al. [51] illustrated the bluff train and ground models, all of which satisfied the standard EN 14067−6 [52].

Fig. 4(c) and (d) show the streamlined train model and ground configuration. Half a downstream vehicle was placed next to the test model (denoted as STV). The ratio of the total length of the train model to the width of the tunnel was less than 0.75. The separation between the adjacent vehicles was 4 mm. The distance from the upstream end of the subgrade to the leading end of STV is 578 mm (11.56 m in full-scale dimensions), which was larger than 8 m in full-scale dimensions. The streamlined train and ground models were the same as our previous work [30] and satisfied the standard EN 14067−6 [52].

Mechanical contact between the wheels and rail was excluded by cutting the base of the wheel in the wind tunnel tests and numerical simulations.

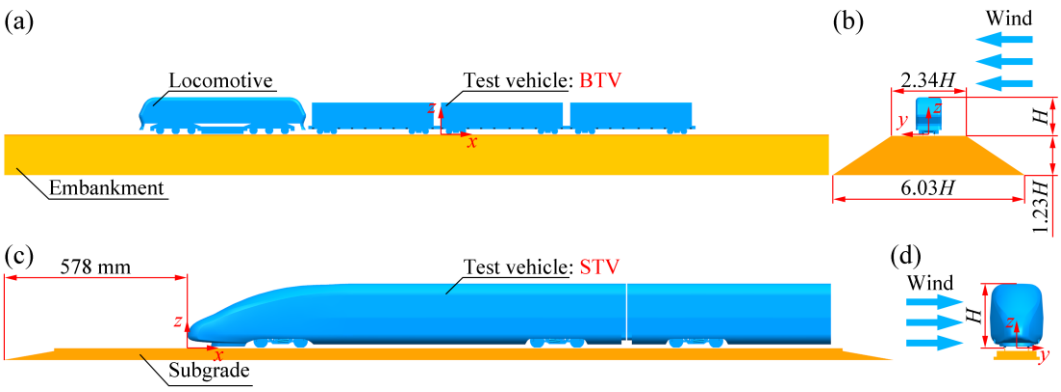

Fig. 4. Train models and ground configurations: (a) side view and (b) front view of bluff train, and streamlined train model: (c) side view and (d) front view of streamlined train.

Unfortunately, Gao et al. [51] did not illustrate the measurements in the wind tunnel tests of BTV. The measurements in the wind tunnel tests of STV were the same as our previous work [30]. The wind speed was measured using a Pitot tube upstream of the model where the wind speed was not affected by the vehicle model and its environment. The pressure scanner had a range of 10 in WC and an accuracy of ±0.10% full-scale. The aerodynamic forces were measured using a force balance, whose range, precision, and accuracy are listed in Table 2. The air density was calculated from the measured temperature and pressure.

Table 2 Parameters of force balance.

Aerodynamic forces	Range	Precision	Accuracy
F_y	1000 N	0.03%	0.09%
F_z	1000 N	0.03%	0.12%

The Reynolds' numbers (Re) in the wind tunnel tests of BTV and STV were 1.30×10^6 and 5.55×10^5, respectively, which could ensure the flow similarity between the model and full-scale flows. Re is defined as

$$Re = \frac{\rho v H}{\mu} \tag{11}$$

where ρ is the air density, v is the wind speed, and μ is the dynamic viscosity.

The results of BTV were nearly Re independent over the range $[0.50Re_{\max}, Re_{\max}](Re_{\max} = 1.30 \times 10^6)$. Fig. 5 illustrates the mean side force and lift coefficients of STV for different Re at the yaw angle of 90°, where $\overline{C}_{Fy}$ and $\overline{C}_{Fz}$ are the mean side force and lift coefficients, respectively. There are error bands in the figure. The average values for the experimental uncertainties associated with the mean side force and lift coefficients were 0.028 and 0.040, respectively. Re ranged from $0.41Re_{\max}$ to $Re_{\max}$ ($Re_{\max} = 5.67 \times 10^5$). The mean side force and lift coefficients remained unchanged, for Re over 3.47×10^5, showing no significant differences for different Re (at the 0.3% level).

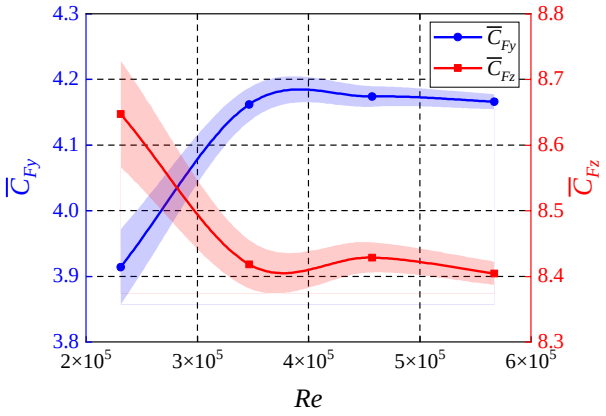

Fig. 5. Aerodynamic force coefficients for different Reynolds numbers.

3.2. Computational method and turbulence modelling

Improved delayed detached-eddy simulation (IDDES) can accurately simulate complex turbulent flows at high *Re* by activating Reynolds-averaged Navier-Stokes equations (RANS) and large eddy simulation (LES) in different flow regions. It significantly improves the application effect of detached-eddy simulation (DES) and delayed one (DDES) in recirculation regions and flow separation and is simple in implementation, cost-free, and robust, refer to Shur et al. [53] for a detailed description. The shear stress transport (SST) k-ω turbulence model combines the advantage of the k-ω model in the boundary layer and the k-ε model in the separation region [54,55]. Morden et al. [56] recommended that the SST k-ω model would be optimal when looking at the surface pressure. It has been demonstrated to be capable of reproducing a complex flow with strong separations [57]. IDDES based on the SST k-ω turbulence model has been used to simulate the flow around trains in crosswinds [5,58–61], whose results were reliable. Therefore, IDDES based on the SST k-ω turbulence model was used to model the viscous, turbulent, unsteady, three-dimensional, and strongly separated flows around the bluff and streamlined trains in crosswinds. The physical time step was set to 1×10^{-4} s so that the Courant number was about 1.

3.3. Computational domain and boundary conditions

Fig. 6 shows the computational domains and boundary conditions of BTV and STV. Fig. 6(a) and (c) include the overhead views of the train models. The width and height of the domain equaled those of the wind tunnel, while the domain extended in the streamwise direction. The blockage ratio was smaller than 5%.

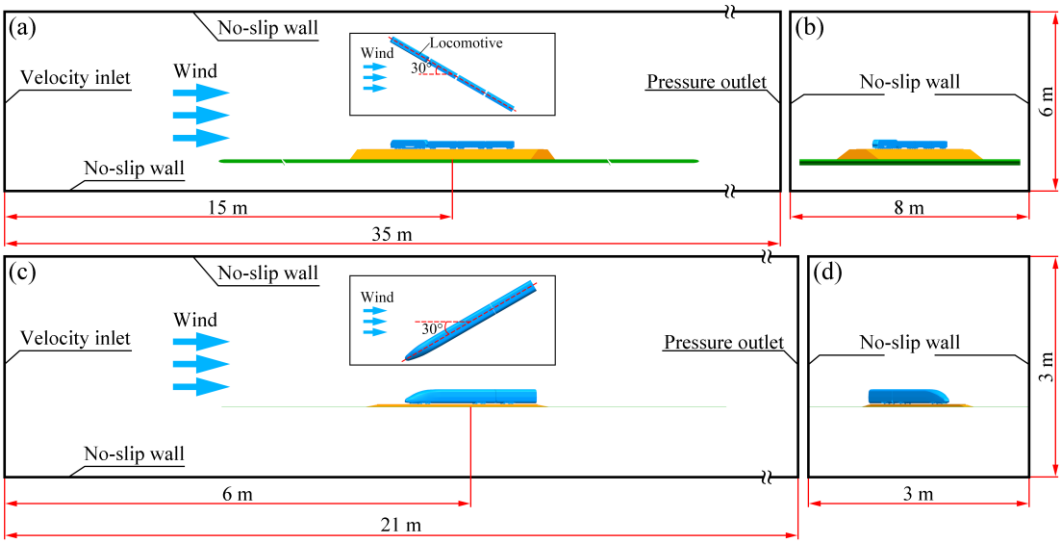

Fig. 6. Computational domain and boundary conditions of BTV: (a) side view and (b) front view and STV: (c) side view and (d) front view.

The front end of the computational domain was the velocity inlet, which had a uniform, i.e., block, profile. The flow speed was independent of the height above ground, except for a thin boundary layer on the domain bottom. *Re* at the velocity inlet of BTV and STV were 1.29 × 10^6 and 5.52 × 10^5, respectively, approximating to the wind tunnel tests. The back end of the domain was the pressure outlet with a boundary pressure of 0 Pa. The sides, roof, and bottom of the domain were the no-slip walls consistent with the wind tunnels. The surfaces of the train and ground models and plates were treated as the no-slip walls. The middle of the bluff train was 15 m away from the velocity inlet and 20 m to the pressure outlet. The middle of the streamlined train were 6 m and 15 m away from the velocity inlet and pressure outlet, respectively.

3.4. Computational mesh and validation

Fig. 7 shows the computational meshes of BTV and STV, which were the trimmed meshes. There were two refinement boxes (Fig. 7(a) and (b) for BTV, as well as (e) and (f) for STV) around the test vehicles to capture the regions of high pressure/velocity gradient such as the vortices and recirculation cells. The blue and red frames represent the refinement box 1 and 2 in the figure, respectively, which were based on BTV and STV. The mesh resolution of the refinement box 2 was higher than that of the refinement box 1. The numbers of cells around the vehicle and between the vehicle and boundaries were sufficient. There were prism layer meshes on the no-slip wall, as shown in Fig. 7(c) and (g), which appropriated for the selected computational method and turbulence model in Section 3.2. As recommended by SIEMENS [55], the thicknesses of the first cell layers on the surface of BTV and STV were 2.59 × 10^{-6} m and 8.82 × 10^{-6} m, respectively, so that their dimensionless wall distances $y+$ were less than or

nearly 1, as shown in Fig. 7(d) and (h). $y+$ in the previous studies was of the same order of magnitude [58,59,61].

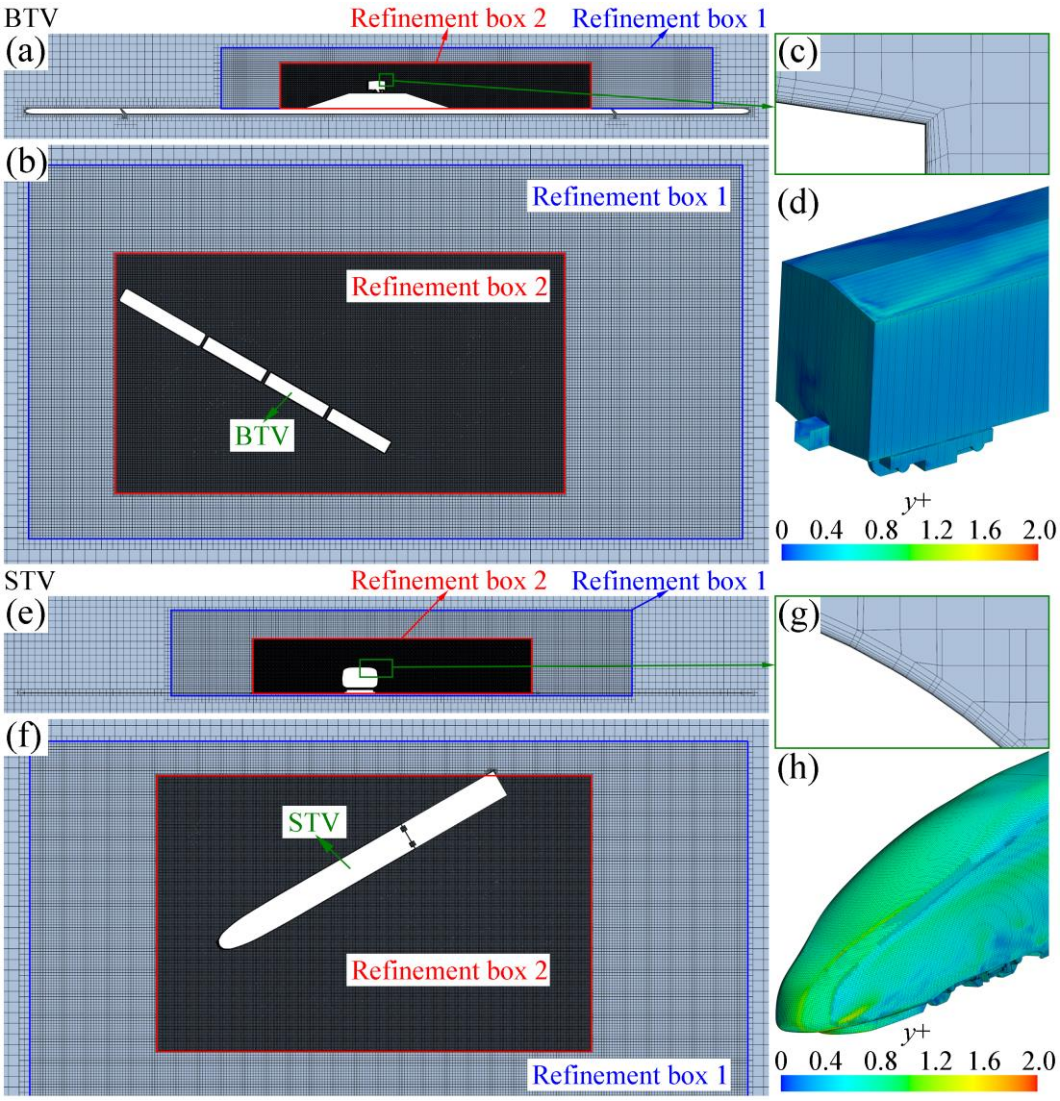

Fig. 7. Computational mesh for BTV: (a) side view, (b) top view, (c) boundary layers, and (d) dimensionless wall distance $y+$, and for STV: (e) side view, (f) top view, (g) boundary layers, and (h) dimensionless wall distance $y+$.

The mesh independencies for BTV and STV were proven by changing the mesh resolution. Fig. 8 illustrates the mean side force and lift coefficients of BTV and STV with three mesh resolutions (coarse, medium, and fine meshes) and those measured in the wind tunnel tests in Section 3.1. The computational mesh shown in Fig. 7 is the medium mesh. The numbers of the cells are listed in Table 3. The mean aerodynamic force coefficients with the coarse mesh differed by large from those with the medium and fine meshes, while the coefficients with the medium mesh were in general agreement with the fine mesh. The mean aerodynamic force coefficients had an accuracy higher than 1.3% between the medium and fine meshes. Fig. 9 illustrates the mean pressure coefficients on the cross-sections of BTV and STV, where $\overline{C}_p$ is

399 the mean pressure coefficient, and WWS and LWS represent the windward and leeward sides
400 of the vehicles. Fig. 9(a1) shows the cross-section of BTV. The blue point begins at the position
401 in the figure and rotates counterclockwise. The distance traveled by the blue point is c in Fig.
402 9(a2), and the perimeter of the section is C. Fig. 9(b1) shows the cross-section of STV, which
403 is the Loop-8 in Gu et al. [30]. The blue point begins at the position in the figure and rotates
404 clockwise, of which the rotation angle is α in Fig. 9(b2). The difference among the mean
405 pressure coefficients with the different mesh resolutions was similar to the mean aerodynamic
406 force coefficients. The coefficients with the medium mesh approximated to those with the fine
407 mesh, and the differences were slightly clear near the transition among the windward side, roof,
408 leeward side, and bottom. The mean side force coefficient, which most affected the running
409 safety of the vehicle [15,43,62], with the medium mesh was larger than that with the fine mesh,
410 and the medium mesh could economize the resource of computer. Therefore, the pressure and
411 aerodynamic load coefficients with the medium mesh were taken as the result.

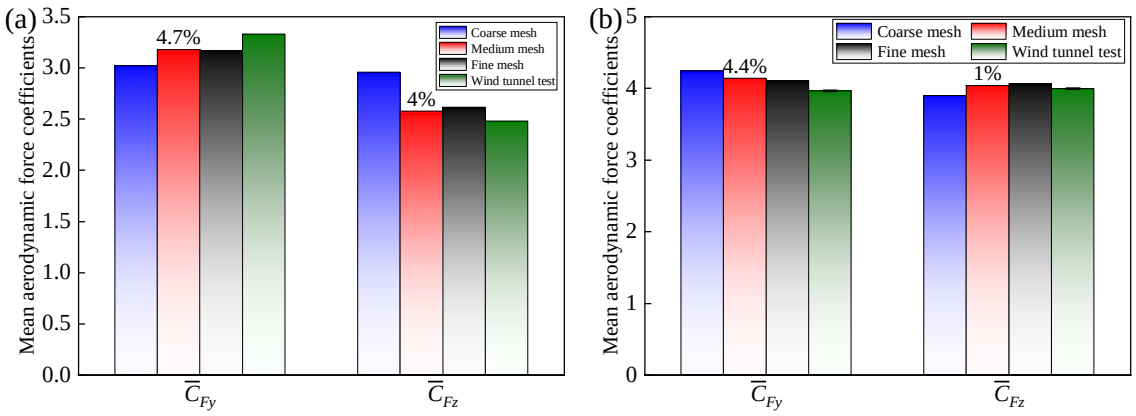

412

413 **Fig. 8.** Mean aerodynamic force coefficients with different mesh resolutions and in wind tunnel tests for (a)
414 BTV and (b) STV.

415 **Table 3** Total numbers of cells with different mesh resolution.

Test vehicle	Coarse mesh	Medium mesh	Fine mesh
BTV	37 million	62 million	90 million
STV	34 million	49 million	73 million

416 Fig. 8 illustrates the errors (the numbers above the red bars) between the mean
417 aerodynamic force coefficients with the medium mesh and those measured in the wind tunnel
418 tests. The maximum error was 4.7%. It is worth noting that the characteristic area to calculate
419 the aerodynamic force coefficients in Section 2.3 is different from that in Gao et al. [51]. The
420 coefficients in Fig. 8(a) have been converted by the characteristic area ratio. The wind tunnel
421 test of STV was included in the wind tunnel campaign at three separated facilities in Li et al.
422 [63], whose results showed a good consistency of the aerodynamic force coefficients measured
423 at the three wind tunnels. The error bars on the green bars in Fig. 8(b) indicate the uncertainties

of the mean aerodynamic force coefficients, which associated with the mean side force and lift coefficients were 0.010 and 0.014, respectively. Fig. 9(b1) and (b2) illustrate the mean pressure coefficient and taps in the wind tunnel test of STV. The mean pressure coefficient with the medium mesh was close to that in the wind tunnel test, although there were still differences at individual taps, which might have been due to the errors of their positions and orientations in the test.

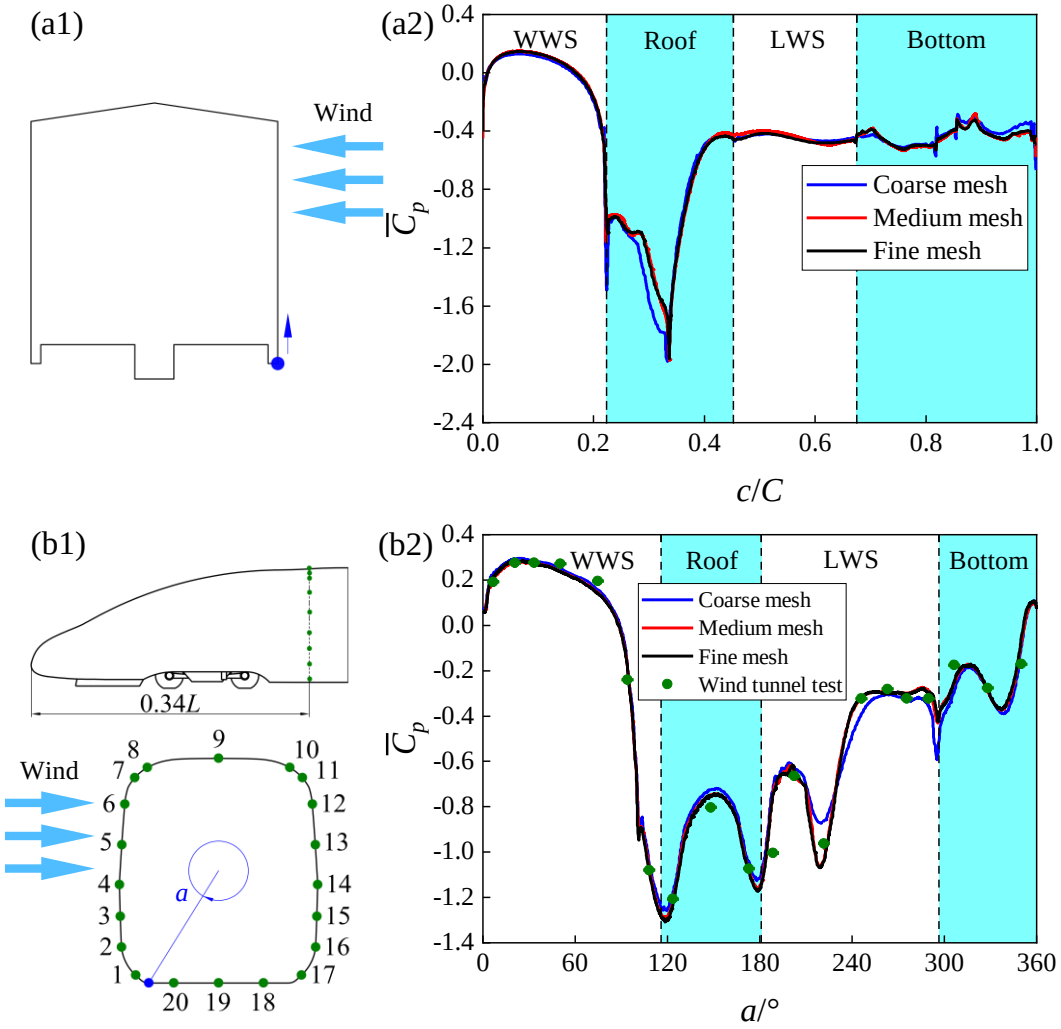

Fig. 9. Mean pressure coefficients on cross sections with different mesh resolutions: cross sections of (a1) BTV and (b1) STV and mean pressure coefficients of (a2) BTV and (b2) STV.

4. Results and discussion

4.1. Discretization of bluff vehicle surface

The strategy of the discrete integration in Section 2 is based on the Lagrange rectangular elements, whose shape function is the product of the Lagrange polynomials, that is, its interior is linear. The linear characteristics of the pressure coefficient on the vehicle surface were studied with the principle of piecewise linearity to evaluate the adaptability and maximum size of the

elements.

The surface pressure distribution of the bluff vehicle did not change a great deal along the length besides both ends of the vehicle [6]. Hence the cross section X1−X1 that is in the middle of BTV is analysed to study the lateral and vertical discretization of the bluff vehicle surface. Fig. 10 illustrates the mean pressure coefficient on the cross section X1−X1 of BTV, where $\overline{C}_{py}$ and $\overline{C}_{pz}$ are the projections of the mean pressure coefficient to the *y*- and *z*-axis, respectively. There are changepoints of the mean pressure coefficient in the figure to determine the maximum size of the Lagrange rectangular elements, which partition the mean pressure coefficient curves into different segments that are best fit by different straight lines. The changepoints were searched by the parametric global method, where the locations of the division points were varied until the total residual error attained a minimum [64–66]. The positions close to both ends of the vehicle were ignored when determining the changepoints. The mean pressure coefficient changed so rapidly there that the Lagrange rectangular elements were not capable of capturing them well. Fortunately the pressure there actually had little effect on the aerodynamic loads of the vehicle.

Fig. 10(b) illustrates the mean pressure coefficient and changepoints on the windward and leeward sides of the cross section X1−X1, where the blue and green frames represent the windward and leeward sides, respectively. The windward side of the main beam, $z < 0.24H$, exhibited a negative pressure, and the mean pressure coefficient increased with the increase in *z*. This might have been due to the vortices on the embankment, which were reported at the height of the top of the rails [67]. The windward side of the roof, at $z > 0.77H$, experienced a negative pressure, and the mean pressure coefficient showed a trend of first increasing and then decreasing and finally increasing with the increase in *z*. The largest mean pressure coefficient was -1.045 around the transition between the windward side and roof, at $z = 0.94H$. The position of the maximum negative pressure was similar to that observed by the previous studies [6,47]. The minimum distance between the changepoints on the windward side was 1197 mm, which partitioned the curve into four segments. A negative pressure appeared on the leeward side, whose variation was caused by the vortices. The minimum distance between the changepoints on the leeward side was 1033 mm. The changepoints partitioned the curve into four segments similar to those on the windward side.

Fig. 10(c) illustrates the mean pressure coefficient and changepoints on the bottom and roof of the cross section X1−X1, where the blue and green frames represent the bottom and roof, respectively, and *W* is the width of BTV. The bottom was a negative pressure region, where the mean pressure coefficient showed a trend of first decreasing and then increasing and finally decreasing. This was related to the vortices separated from the apron board and main-beam of

the vehicle. The minimum occurred was -0.284 at y = -0.10W, while the largest value was -0.532 at y = 0.20W. The changepoints approximately divided the mean pressure coefficient curve into three equal segments. On the bottom of the vehicle, unlike on the windward side, leeward side, and roof, the geometric detail of the vehicle led to the pressure variation. Hence the dimensionless distance between the changepoints − rather than the absolute distance − made sense on the bottom. The mean pressure coefficient was negative on the roof and was partitioned into two segments by the changepoints. The trend of first slow increasing and then sharp decreasing was similar to that in Flynn et al. [4].

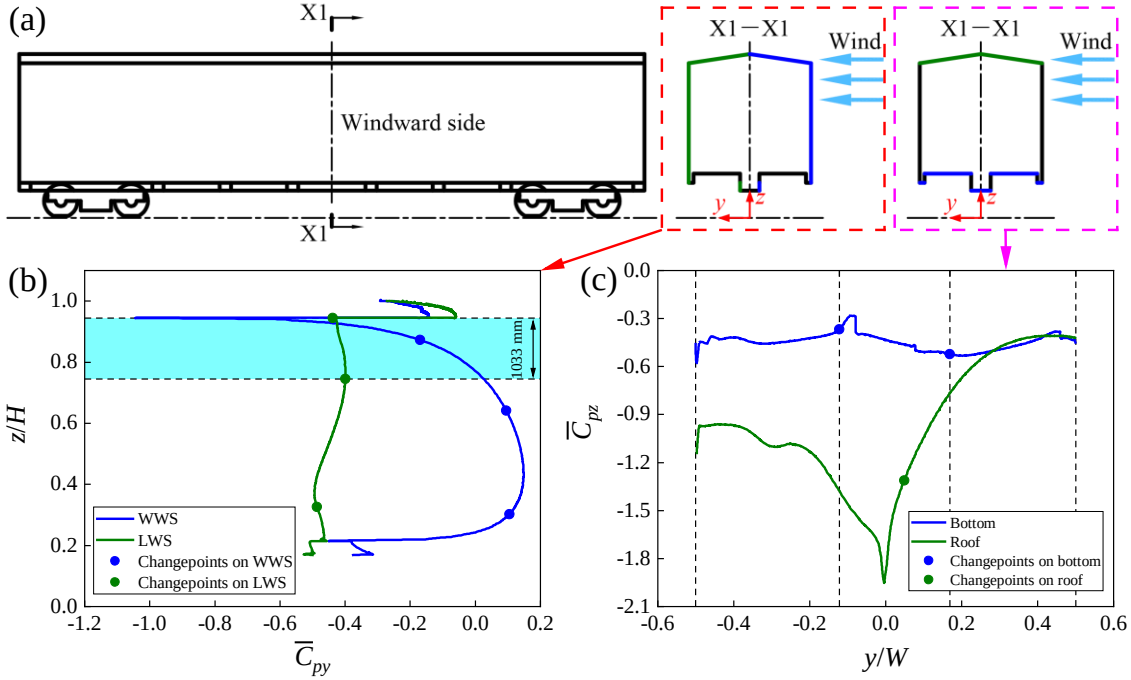

Fig. 10. Mean pressure coefficients on cross section of BTV: (a) position of cross section X1−X1 and mean pressure coefficients on (b) WWS and LWS, as well as (c) bottom and roof.

To summarise, for convenience, the bluff vehicle should be divided into at least three and four Lagrange rectangular elements in the lateral and vertical directions, respectively. The maximum vertical length of the elements should be 1000 mm.

BTV was divided into three and four Lagrange rectangular elements in the lateral and vertical directions, respectively, as mentioned above. The vertical length of the elements was less than 1000 mm. Fig. 11(a) shows the horizontal cross sections Z1−Z1, Z2−Z2, Z3−Z3, and Z4−Z4 at the midpoints of the vertical elements, and Fig. 12(a) shows the vertical sections Y1−Y1, Y2−Y2, and Y3−Y3 at the midpoints of the lateral elements.

Fig. 11(b)−(e) illustrate the mean pressure coefficients and changepoints on the windward and leeward sides of the horizontal cross sections, where L is the length of BTV. The mean pressure coefficients on the windward side numerically showed trends of first decreasing and then increasing and finally decreasing. The coefficients changed slightly in the middle of the

vehicle but changed significantly near the ends. The pressure variations in the middle of the vehicle might have been caused by the following factors. The flow was slightly deflected for the yaw angle when crossing the windward slope of the embankment, influencing the flow acceleration near the transition between the windward side and roof of the vehicle, the flow acting on the vehicle directly, and the vortices separating from the windward slope. The mean pressure coefficients were negative on the leeward side and slowly decreased along the length of the vehicle, which might have been caused by the vortices separating from the vehicle and moving downstream in crosswinds. Similar results were found by Hemida and Baker [6]. The minimum distance between the changepoints on the windward on leeward sides was 4412 mm, and the changepoints partitioned the curves on the windward and leeward sides into three and four segments, respectively.

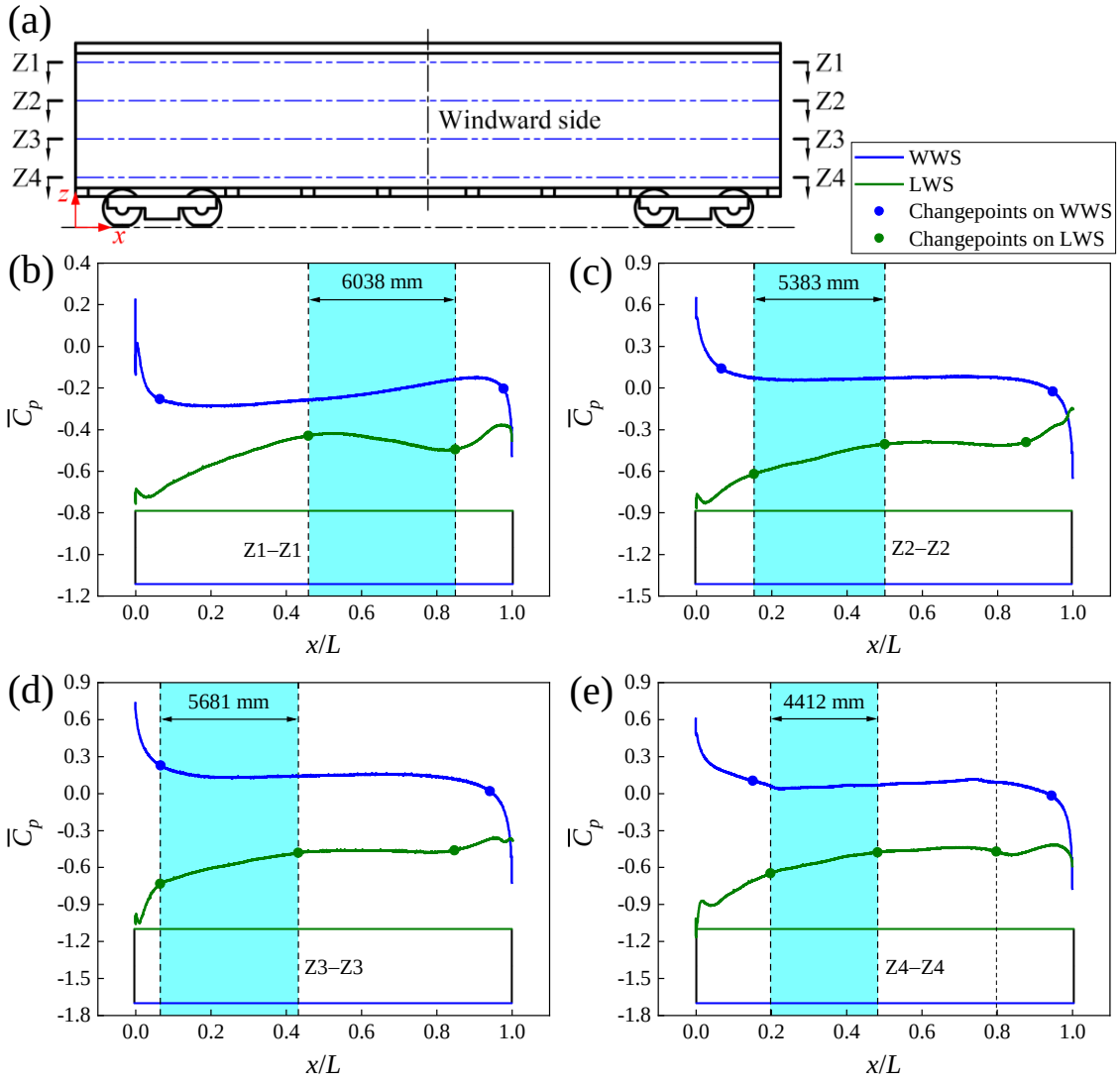

Fig. 11. Mean pressure coefficients on horizontal cross sections of BTV: (a) positions of horizontal cross sections and mean pressure coefficients on horizontal cross section (b) Z1−Z1, (c) Z2−Z2, (d) Z3−Z3, and (e) Z4−Z4.

Fig. 12(b)−(d) illustrate the mean pressure coefficients and changepoints on the bottom and roof of the vertical sections. The mean pressure coefficients presented dramatic changes on the bottom, which might have been due to the complex geometry [6], especially the bogies. The coefficients generally remained unchanged along the length of the vehicle − just fluctuated around some values. The dimensionless distance between the changepoints was meaningful compared with the absolute distance on the bottom, as mentioned above. The changepoints partitioned the curves into three segments, which were two bogie regions and a middle region. The roof exhibited negative pressures, and the mean pressure coefficients showed trends of first increasing and then decreasing. The largest value -1.622 occurred at $x = 0.17L$ on the vertical section Y1−Y1, and the maximum -2.003 occurred at $x = 0.53L$ on the section Y2−Y2, as well as the largest value was -1.009 at $x = 0.82L$ on the section Y3−Y3. The position of the maximum pressure on the roof moved rearward with the increase in the distance between the vertical section and windward side, which might have been caused by the yaw angle. The minimum distance between the changepoints on the roof was 4277 mm, which partitioned the curves into four segments.

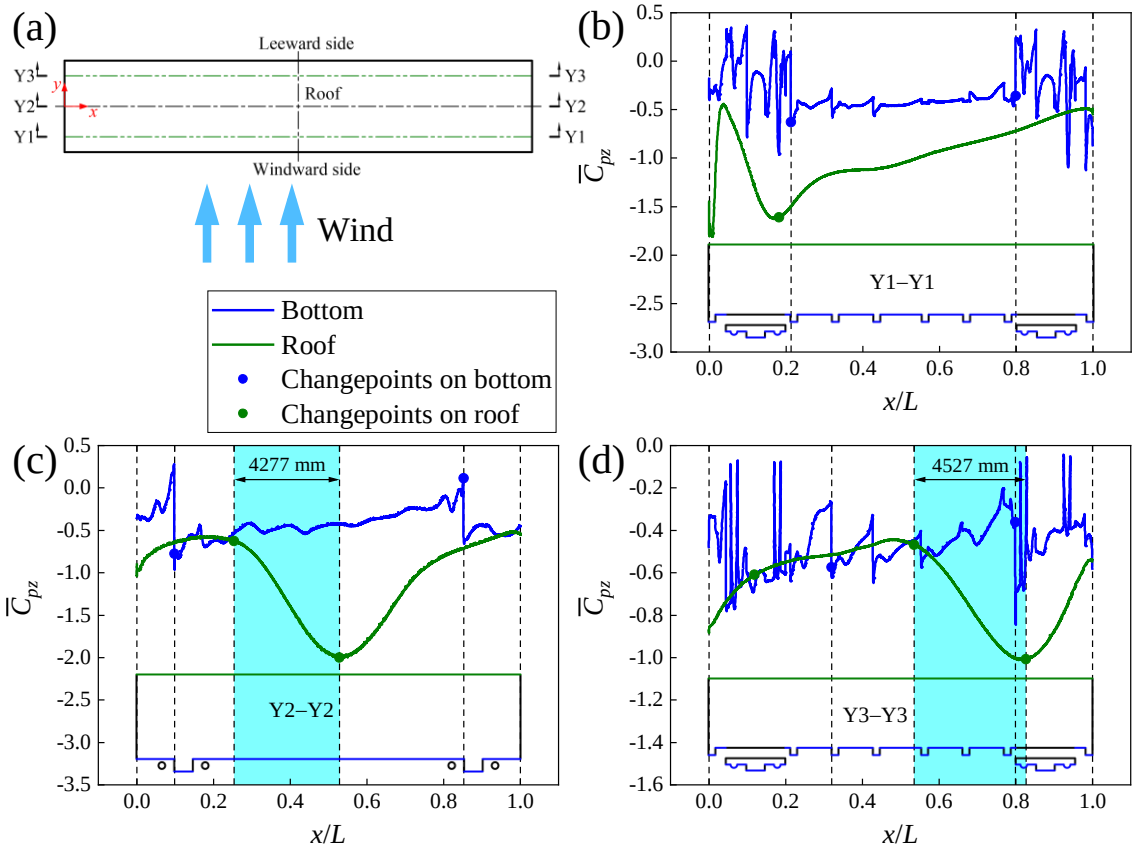

Fig. 12. Mean pressure coefficients on vertical sections of BTV: (a) positions of vertical sections and mean pressure coefficients on vertical section (b) Y1−Y1, (c) Y2−Y2, and (d) Y3−Y3.

The regions with the significant variations in the mean pressure coefficients on the roof corresponded to the bogies on the vertical section Y1−Y1 and Y3−Y3, as shown in Fig. 12(b)

and (d). Thus the bottom and roof could be divided into three or four segments for capturing the mean pressure coefficients in the longitudinal direction. However, on the section Y2−Y2, the region with the significant variation in the mean pressure coefficient on the roof was matched with the middle of the bottom, as shown in Fig. 12(c). Hence, the bottom and roof should be divided into five segments.

To summarise, the bluff vehicle should be divided into at least five Lagrange rectangular elements, whose maximum longitudinal length of the elements should be 4250 mm, in the longitudinal direction.

4.2. Discretization of streamlined vehicle surface

The shape of the streamlined vehicle body which excludes the streamlined head is similar to that of the bluff vehicle, whose discretization could refer to the discretization of the bluff vehicle surface in Section 4.1.

Fig. 13 illustrates the mean pressure coefficients on the cross section X2−X2 of STV, which is in the middle of the vehicle body. STV was divided into three and four Lagrange rectangular elements in the lateral and vertical directions, respectively, as mentioned in Section 4.1. Fig. 13(a) shows the pressure taps at the midpoints of the elements.

Fig. 13(b) illustrates the mean pressure coefficients on the windward and leeward sides and at the taps. On the windward side of the roof, $z > 0.73H$, the vehicle experienced a negative pressure, and the mean pressure coefficient showed a trend of first increasing and then decreasing with the increase in z. Similar results were found by Guo et al. [58] and Huo et al. [59]. The largest value occurred around the transition between the windward side and roof, at $z = 0.93H$, which might have been due to the flow acceleration [68], similar to the trend of BTV shown in Fig. 10. The mean pressure coefficient was negative on the leeward side. The coefficient varying was complex. This was because the flow, detaching from the roof, mixed with the flow that blew over the streamlined head, giving rise to complex three-dimensional vortices [13].

Fig. 13(c) illustrates the mean pressure coefficients on the bottom and roof and at the taps. The mean pressure coefficient on the bottom was positive near the windward side, at $y < -0.25W$, which showed a trend of first increasing and then decreasing. The peak value occurred at $y = -0.42W$, which might have been related to the windward rail [69]. The mean pressure coefficient was negative at $y > -0.24W$, and it showed a trend of first increasing and then decreasing. The maximum -0.638 appeared at $y = 0.37W$. The maximum negative pressure might have been caused by the vortices behind the leeward rail [69]. A negative pressure appeared on the roof, and the mean pressure coefficient showed a trend of first increasing and then decreasing. The

largest value of the coefficient occurred around the transition between the windward side and roof, at $y = -0.32W$, as mentioned above, where the flow velocity was accelerated and there was a strong negative pressure.

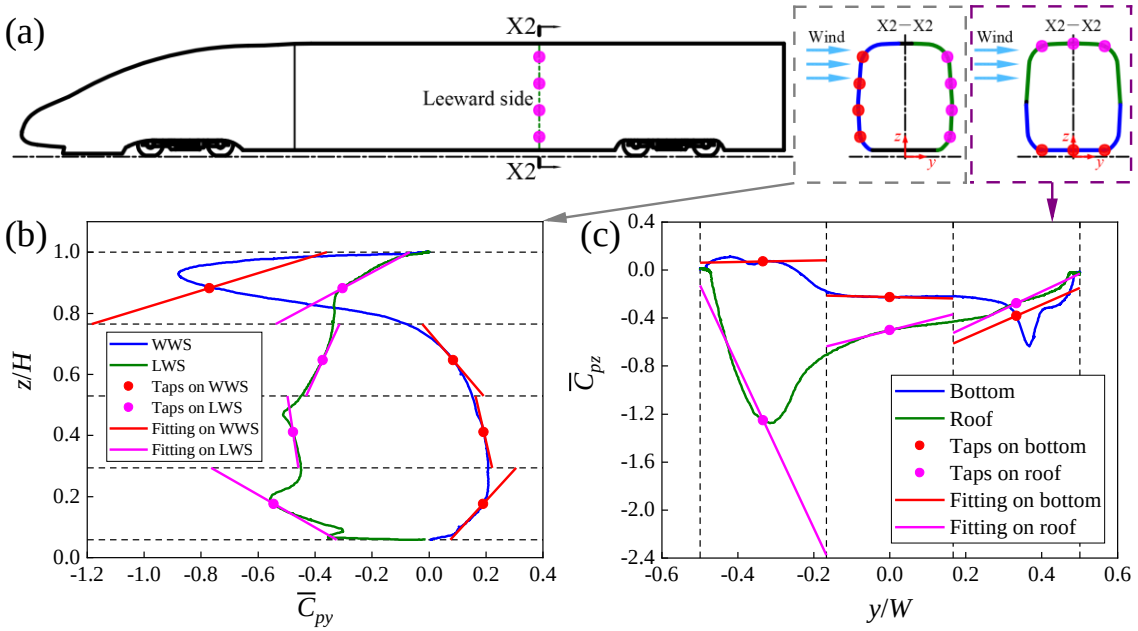

Fig. 13. Mean pressure coefficients on cross section of STV: (a) position of cross section X2−X2 and mean pressure coefficients on (b) WWS and LWS, as well as (c) bottom and roof.

The linear least-squares data fitting was carried to the mean pressure coefficients in the elements on the cross section X2−X2, and the fitting straight lines should pass by the mean pressure coefficients at the midpoints of the elements. The red and magenta lines are the fitting lines on the windward and leeward sides in Fig. 13(b), and ones are the fitting lines on the bottom and roof in Fig. 13(c). The linearities of the mean pressure coefficients were evaluated by the coefficient of determination R^2. The closer R^2 was to 1, the higher the linearity was, though this was not the original meaning of R^2, which is defined as

$$R^2 = 1 - \frac{SS_{\text{res}}}{SS_{\text{tot}}} \tag{12}$$

where SS_{res} is the total sum of squares, and SS_{tot} is the residual sum of squares.

The linearities of the mean pressure coefficients of the most elements were relatively high on the cross section X2−X2. The maximum R^2 was 0.9047, while the peak value of R^2 in the elements was 0.9453. Only the elements near the transition between the windward side and roof were with low linearity, as mentioned above, but they made a small contribution for the aerodynamic loads. Therefore, the lateral and vertical discretization of the bluff vehicle in Section 4.1 applied to that of the streamlined vehicle body. The vertical discretization of the streamlined vehicle body was the same as that in Liu et al. [48], which was divided into four elements. Moreover, as mentioned by them, the aerodynamic loads did not significantly

589 improve with a small increase in the number of the elements in the vertical direction. This was
590 the inevitable result caused by the mean pressure distribution of the streamline vehicle body
591 according to the results above.
592 The vehicle body of STV was divided into five Lagrange rectangular elements in the
593 longitudinal direction, as mentioned in Section 4.1. In the lateral and vertical directions, it fell
594 into three and four elements, respectively, as shown in Fig. 13. To study the longitudinal
595 discretization of the streamlined head, the horizontal cross sections Z5−Z5, Z6−Z6, Z7−Z7, and
596 Z8−Z8 at the midpoints of the vertical elements, as shown in Fig. 14(a), are analysed, as well
597 as the vertical sections Y4−Y4, Y5−Y5, and Y6−Y6 at the midpoints of the lateral elements, as
598 shown in Fig. 15(a).
599 Fig. 14(b)−(e) illustrate the mean pressure coefficients on the windward and leeward sides
600 and at the taps on the vehicle body. The windward side of the horizontal section Z5−Z5 was a
601 negative pressure region, which was around the transition between the windward side and roof,
602 as shown in Fig. 13(b). The mean pressure coefficient was negative on the leeward side and
603 showed a trend of first increasing and then decreasing and finally becoming stable. The largest
604 value occurred at $0.05L < x < 0.27L$. The positions of the maximum pressures on the windward
605 and leeward side moved forward with the lowering in the horizontal sections. Apart from the
606 section Z5−Z5, the maxima of positive and negative pressures appeared on the windward and
607 leeward side of the streamlined head, respectively, as mentioned by Zhang et al. [68].
608 The red and magenta lines are the fitting lines on the windward and leeward sides of the
609 vehicle body in Fig. 14(b)−(e). The linearities of the mean pressure coefficients on the
610 windward and leeward sides of the vehicle body were high. The average value for R^2 was 0.9145,
611 and the maximum was 0.9999. The largest value of R^2 in the elements was 0.9895. Therefore,
612 the longitudinal discretization of the bluff vehicle in Section 4.1 could be applied across the
613 streamlined vehicle body.
614 Fig. 14(b)−(e) also illustrate the pressure changepoints on the windward and leeward sides
615 of the streamlined head, where the minimum distance between the changepoints was 2733 mm.

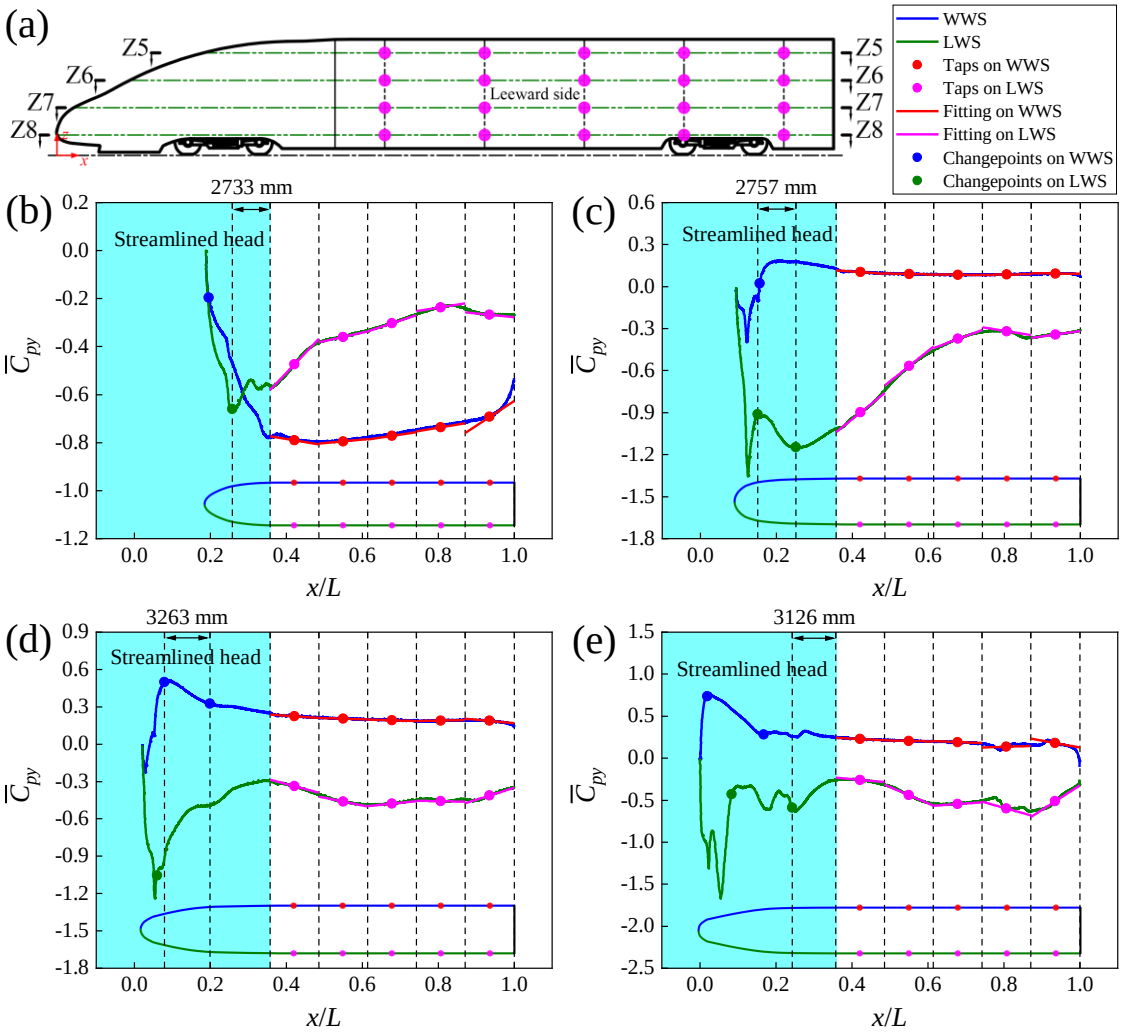

Fig. 14. Mean pressure coefficients on horizontal cross sections of STV: (a) positions of horizontal cross sections and mean pressure coefficients on horizontal cross section (b) Z5−Z5, (c) Z6−Z6, (d) Z7−Z7, and (e) Z8−Z8.

Fig. 15(b)−(d) illustrate the mean pressure coefficients on the bottom and roof and at the taps on the vehicle body. The mean pressure coefficients changed rapidly on the bottom similar to those of BTV. Jiang et al. [69] found that there were abrupt changes in the mean pressure coefficient near the cowcatchers, which might have been related to their geometric shapes. The pressure presented dramatic changes near the bogie cabins, especially when the flow left them, as mentioned by Guo et al. [70]. A positive pressure appeared in some areas near the front end of the vertical section Y4−Y4, which might have been related to the yaw angle, as mentioned in the description of Fig. 12. The rest of the roof was a negative pressure region, and the mean pressure coefficient showed a trend of first increasing and then decreasing. The largest value occurred at $0.13L < x < 0.45L$, of which the position moved forward with the increase in the distance between the vertical section and windward side of STV.

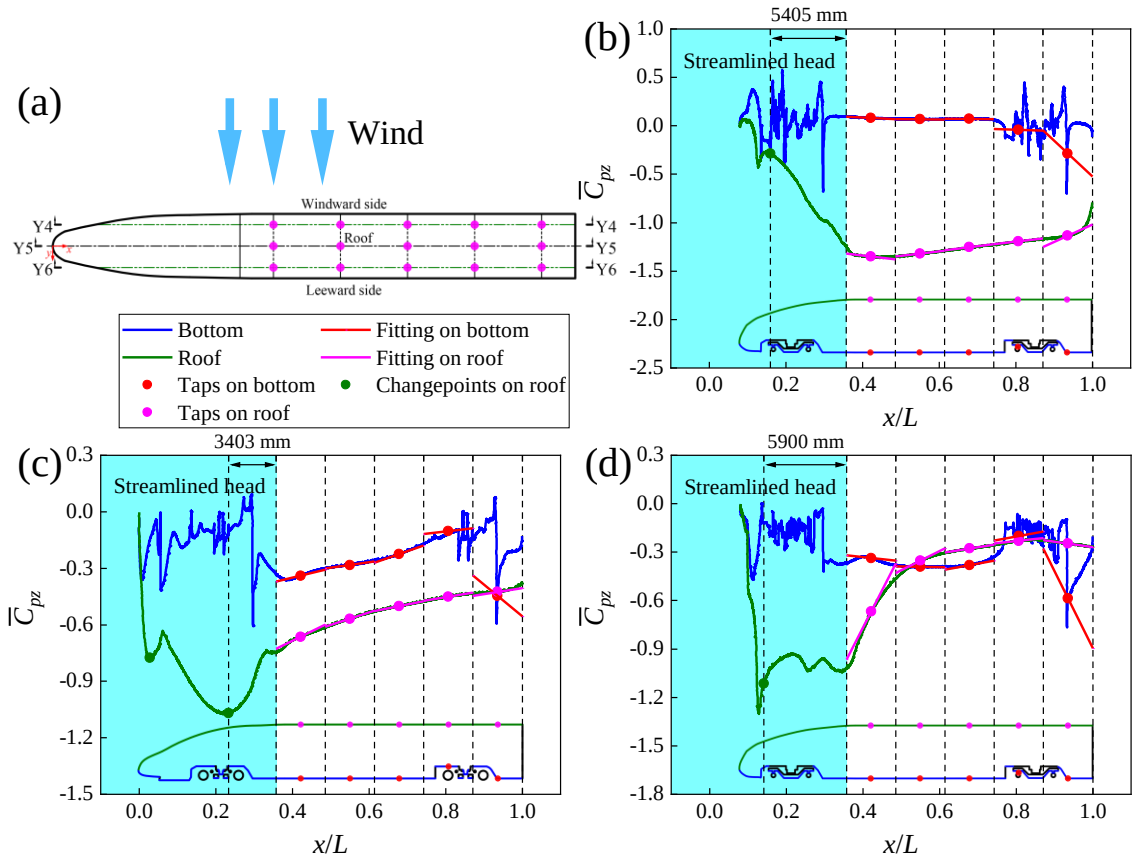

Fig. 15. Mean pressure coefficients on vertical sections of STV: (a) positions of vertical sections and mean pressure coefficients on vertical section (b) Y4−Y4, (c) Y5−Y5, and (d) Y6−Y6.

The red and magenta lines are the fitting lines on the bottom and roof of the vehicle body in Fig. 15(b)−(d). The linearities of the mean pressure coefficients near the bogies were relatively low, which was caused by the chaotic variations of the coefficients [69]. The linearities of the coefficients were high in the middle of the bottom, and the largest value of R^2 was 0.9836 in the elements. Overall the linearities of the coefficients were high on the roof. R^2 of 73.3% of the elements was larger than 0.8816, and the maximum was 0.9973.

Fig. 15(b)−(d) also include the pressure changepoints on the bottom and roof of the streamlined head, where the minimum distance between the changepoints was 3403 mm.

To summarise, the maximum longitudinal length of the Lagrange rectangular elements should be 2700 mm on the streamlined head of the vehicle.

The streamlined head of STV was divided into four Lagrange rectangular elements in the longitudinal direction, as mentioned above. The longitudinal length of the elements was less than 2700 mm. The cross sections X3−X3, X4−X4, X5−X5, and X6−X6 at the midpoints of the longitudinal elements are analysed. The streamlined head was divided into three and four elements in the lateral and vertical directions, respectively, as mentioned above. However, to facilitate realistic testing, the sections X3−X3 and X4−X4 were divided into two and three vertical elements with the same height of the other elements, respectively, since the original

heights of the sections were low. Similarly, the section X3−X3 had only one element in the lateral directions. Fig. 16(a) shows the taps at the midpoints of the vertical elements, and Fig. 17(a) shows those at the midpoints of the lateral elements.

Fig. 16(b)−(e) illustrate the mean pressure coefficients on the windward and leeward side of the cross sections and at the taps. The transition between the windward side and roof of the streamlined head exhibited negative pressures. The mean pressure coefficients showed a trend of first increasing and then decreasing with the increase in z. The maximum negative pressure appeared around the transition between the leeward side and roof, which was similar to the results in Zhang et al. [41].

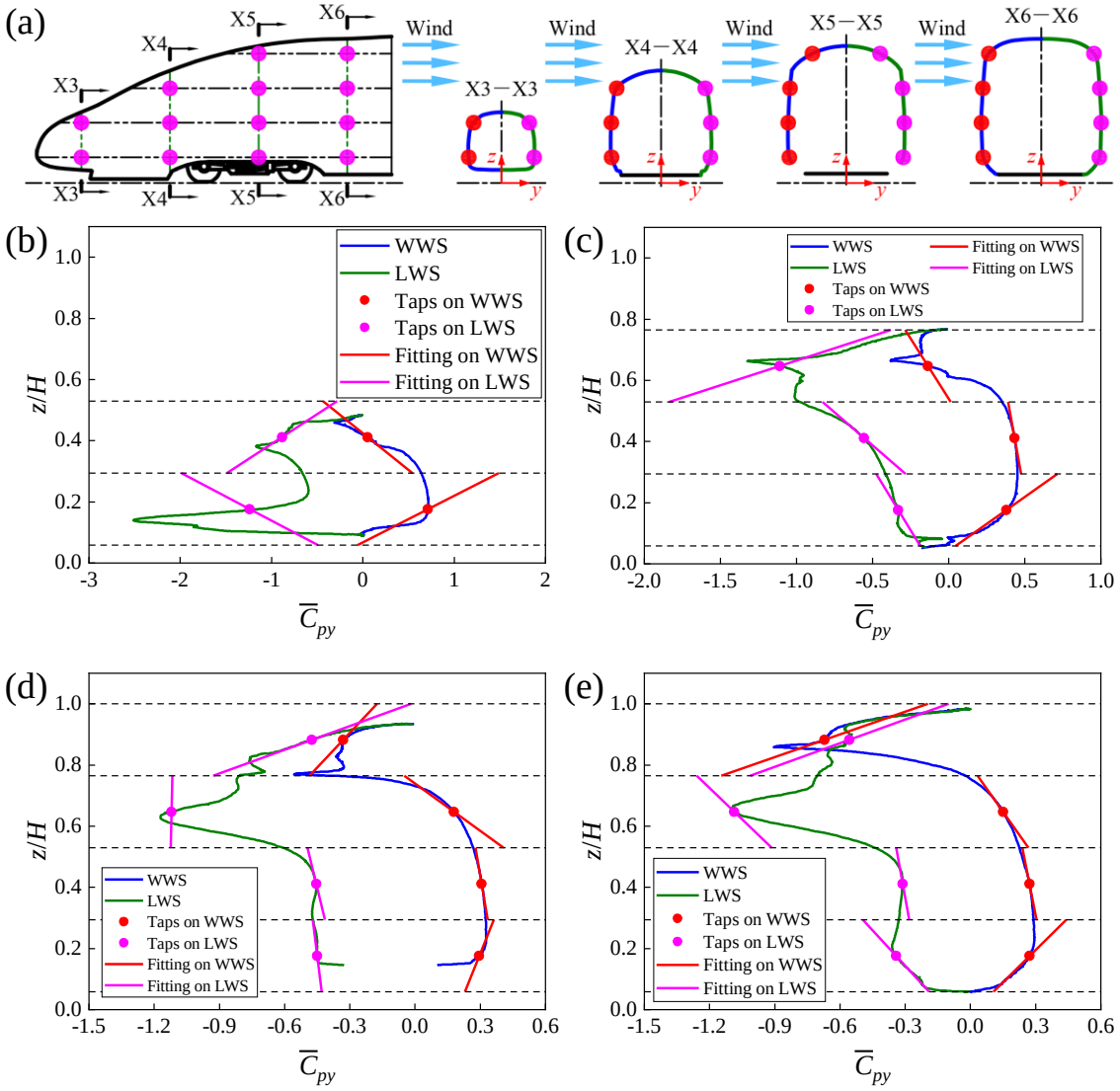

Fig. 16. Mean pressure coefficients on windward and leeward sides of streamlined head: (a) position of cross sections and mean pressure coefficients on cross section (b) X3−X3, (c) X4−X4, (d) X5−X5, and (e) X6−X6.

Fig. 17(b)−(e) illustrate the mean pressure coefficients on the bottom and roof of the cross sections and at the taps. The mean pressure coefficient changed acutely on the bottom of the cross section X3−X3. With the increase in y, the positive pressure was transposed to the

negative one on the bottom, and the mean pressure coefficient showed a trend of first slightly increasing and then significantly decreasing and finally sharply increasing. The mean pressure coefficient was kept essentially constant on the bottom of sections X4−X4, X5−X5, and X6−X6. The roof was a little positive pressure region at y = -0.5W, indicating that the airflow acted on the region directly [41].

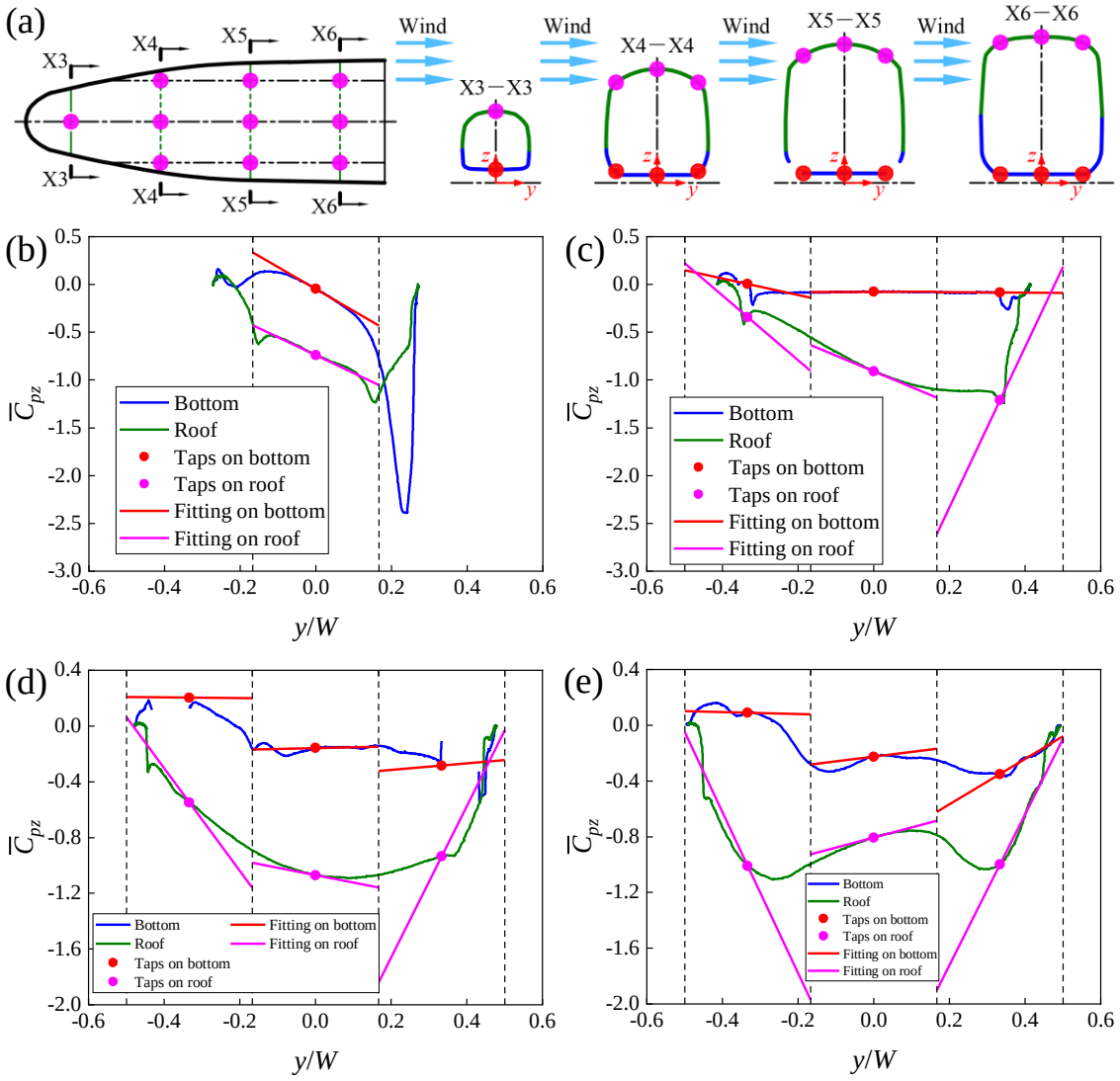

Fig. 17. Mean pressure coefficients on bottom and roof of streamlined head: (a) position of cross sections and mean pressure coefficients on cross section (b) X3−X3, (c) X4−X4, (d) X5−X5, and (e) X6−X6.

The red and magenta lines are the fitting lines on the windward and leeward sides of the streamlined head in Fig. 16(b)−(e), and ones are the fitting lines on the bottom and roof in Fig. 17(b)−(e). The linearities of the mean pressure coefficients were relatively high except individual elements. The average of R^2 was 0.7526, and the maximum was 0.9903. The largest value of R^2 was 0.9472 in the elements. Such linearity could be acceptable, considering the complex variations of the pressure on the streamlined head, especially on the bottom.

Therefore, the lateral and vertical discretization of the streamlined head was the same as

681 that of the vehicle body.

682 **4.3. Mean aerodynamic load coefficients**

683 The discretization of the vehicle surfaces in Sections 4.1 and 4.2 applied to most bluff and
684 streamlined vehicles of similar shapes. BTV and STV were discretized using the strategy of the
685 discretization, as mentioned above, to clear the accuracy of the discretization and discrete
686 integration. Fig. 18 and Fig. 19 show the layout of the taps, which are at the midpoints of the
687 elements, on the BTV and STV, respectively. The layouts on the windward and leeward sides
688 were the same and did ones on the bottom and roof. BTV was divided into five, three, and four
689 elements in the longitudinal, lateral, and vertical directions, respectively. There were 70
690 elements, including 40 elements on the windward and leeward sides and 30 elements on the
691 bottom and roof. STV was divided into nine, three, and four elements in the longitudinal, lateral,
692 and vertical directions, respectively. There were 116 elements, including 66 elements on the
693 windward and leeward sides and 50 elements on the bottom and roof. The above mentioned
694 was the ideal layouts of the taps. In tests, if the locations of the taps were not available, the
695 discretization would remain unchanged, and the taps would move around the midpoints of the
696 longitudinal elements in the longitudinal direction. The principle of moving direction was to try
697 not to change the geometric features around the taps. The eighth longitudinal element moved
698 rearward in Fig. 19 because its midpoint was originally situated on the wheelset.

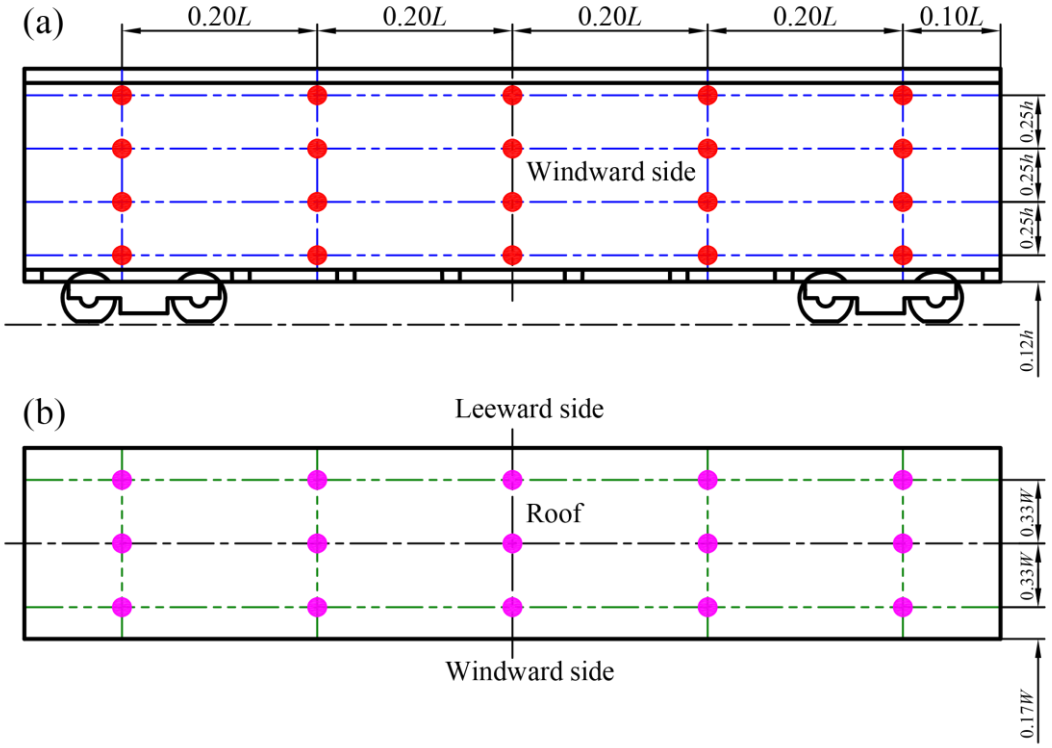

699

700 **Fig. 18.** Layout of taps on BTV: (a) side view and (b) top view.

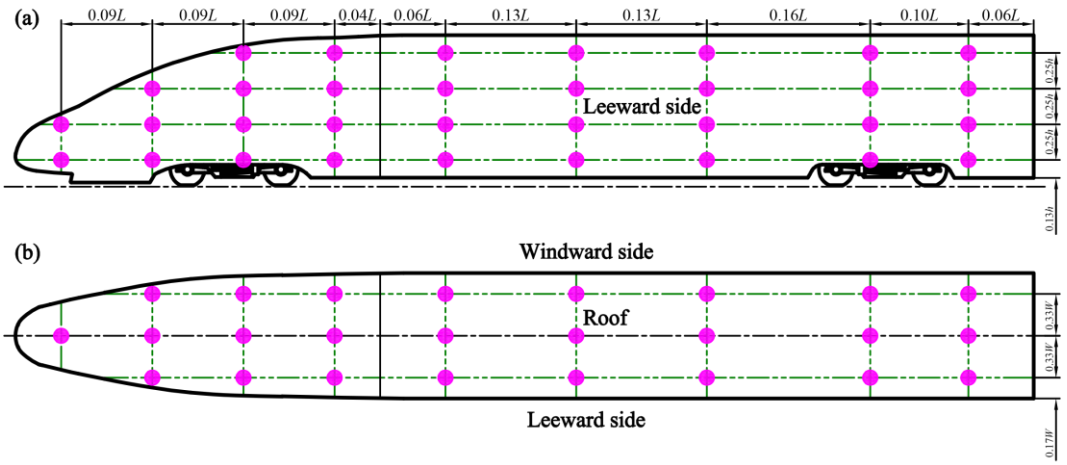

Fig. 19. Layout of taps on STV: (a) side view and (b) top view.

In the model tests, the pressures at the taps would be monitored using pressure scanners, and the aerodynamic loads and surface pressure distribution of the vehicle would be obtained. Of course, a preference for force balances should be stated in the wind tunnel tests (the static model tests). In the full-scale tests, the ranges of absolute pressure transducers that could be used in the tests would be far greater than the variation of the surface pressure on the vehicle in crosswinds. Its resolution would be relatively low. Variations of altitude might also be larger than those of the surface pressures in the full-scale tests. Hence, to obtain the aerodynamic loads, differential piezoresistive transducers with small ranges and high accuracies would be advised to use for measuring the pressure differences between the corresponding taps in the full-scale tests.

The projections of the pressures at the corresponding taps on the windward and leeward sides in y-axis were the same, so the differential piezoresistive transducers could directly measure the side force. However, that would be not the case for the lift, where the projections at the corresponding taps on the bottom and roof in z-axis were different. Fortunately, a quantitative relation between the coefficient $C_{\Delta pz}$ for calculating the lift and the coefficient $C_{\Delta p}$ measured by the differential piezoresistive transducers could be made. Fig. 20 illustrates the relation between the two mean pressure coefficients $\overline{C}_{\Delta pz}$ and $\overline{C}_{\Delta p}$. The relations of BTV and STV were nearly linear between the two coefficients, and R^2 of those were 0.9999 and 0.9912, respectively. The fitting relations could be obtained early by the numerical simulations in the future full-scale tests. There was a simple way of using $C_{\Delta p}$ in place of $C_{\Delta pz}$ since the approximation function was $C_{\Delta pz} = C_{\Delta p}$, whose accuracy would be relatively low.

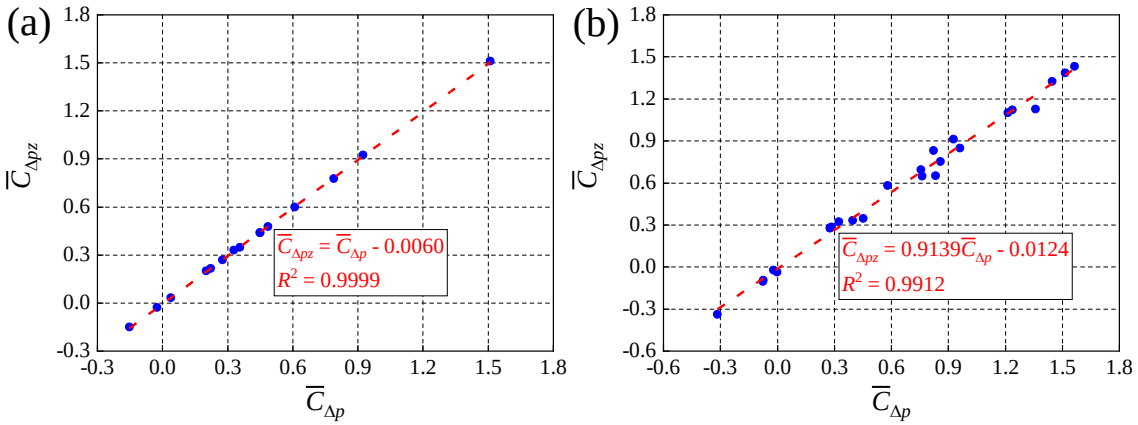

Fig. 20. Mean pressure coefficients on bottom and roof of (a) BTV and (b) STV.

Table 4 lists the mean aerodynamic load coefficients obtained by the discrete integration mentioned above and numerical simulations, as well as the errors between them, indicating the accuracy of the discretization and discrete integration suggested above. It is worth noting that the mean aerodynamic load coefficients obtained by the numerical simulations in the table included the viscous loads. The error of the mean side force coefficient of BTV was the smallest, which was 2.5%, while the mean lift coefficient had the largest error of 12.9%. The linearity of the mean pressure coefficient was relatively low on the bottom of BTV with complicated geometry, leading to a large error in the mean lift coefficient. But such errors could be accepted since the side force most affected the running safety of the vehicle, as mentioned in Section 3.4. The mean aerodynamic load coefficients of STV had little errors, and the maximum error was only 2.2%. The bottom of STV had regular shape due to the equipment cabins, thus the error of the mean lift coefficient was little. The errors of STV were little in general. This might be because the flow separation around STV was suppressed due to the aerodynamic shape, thus the linearity of the mean pressure coefficient was higher than that of BTV.

Table 4 Mean aerodynamic load coefficients and their error.

Mean aerodynamic load coefficients	BTV			STV		
	$\overline{C}_{Fy}$	$\overline{C}_{Fz}$	$\overline{C}_{Mx,\mathrm{lee}}$	$\overline{C}_{Fy}$	$\overline{C}_{Fz}$	$\overline{C}_{Mx,\mathrm{lee}}$
Discrete integration	3.097	2.247	2.233	4.074	3.979	2.566
Numerical simulation	3.176	2.579	2.145	4.142	4.038	2.511
Relative error	2.5%	12.9%	4.1%	1.6%	1.5%	2.2%

The errors in Table 4 were in acceptable range, especially considering the experimental uncertainties. Therefore, the strategies of the discretization and discrete integration suggested above were sufficient to obtain the mean aerodynamic loads on the vehicles in crosswinds. The surface pressure distributions of different bluff vehicles would be similar and so did streamlined vehicles. Hence the strategies could be extended to more vehicles.

The discrete integration (see Section 2) and discretization of the vehicle surfaces (see Sections 4.1 and 4.2) have been improved. The strategies above fit together well. The number of the taps would be relatively small, which was easier to use in the tests, especially in the full-scale tests. The mean aerodynamic load coefficients of BTV and STV were calculated with the method in Gao et al. [18] with the layouts of the taps shown in Fig. 18 and Fig. 19. The suggested strategies significantly improved the accuracies of the mean lift and rolling moment coefficients of the streamlined vehicles, which were increased by 8.7% and 8.4%, respectively, compared with the calculation of the coefficients in the previous studies. However, the errors of the mean lift and rolling moment coefficients of the bluff vehicles reduced by 1.3% and 2.8%, respectively.

The errors in Table 4 were for the yaw angle of 30° (see Section 3.1). Liu et al. [48] indicated that the discrete integration would have approximate equal errors at the yaw angles of 5.87−30°. The errors in the range of 30−90° would be smaller than the maximum error at the yaw angles of less than 30°. Anyway, the yaw angles would be primarily 0−30°, as mentioned in Section 3.1. The errors in Table 4 could be directly used in the full-scale tests and model tests.

4.4. Unsteady aerodynamic load coefficients

The aerodynamic loads on the vehicles in crosswinds were unsteady and fluctuated around the mean values [68]. The reappearance of the unsteady aerodynamic loads was evaluated in this section.

Table 5 lists the amplitudes of the unsteady aerodynamic load coefficients of BTV and STV. The amplitudes of the aerodynamic load coefficients obtained by the suggested strategies were larger than those obtained by the numerical simulations, with an average increase of 0.363, indicating that the fluctuations acquired by the suggested strategies were larger. This might be due to the amplification of the pressure fluctuations at the taps in the strategies. Although the fluctuations of the aerodynamic loads cannot be accurately evaluated in the strategies, the large fluctuations measured were conservative in the running safety of the vehicles [71].

Table 5 Amplitudes of unsteady aerodynamic load coefficients.

Aerodynamic load coefficients	BTV			STV		
	C_{Fy}	C_{Fz}	$C_{Mx,\,\mathrm{lee}}$	C_{Fy}	C_{Fz}	$C_{Mx,\,\mathrm{lee}}$
Discrete integration	1.139	2.167	0.888	0.779	0.514	0.373
Numerical simulation	0.961	1.581	0.485	0.280	0.245	0.129

Fig. 21 illustrates the normalized cross-correlation (NCC) of the aerodynamic load coefficients of BTV and STV, where τ is the time lag. The largest values of NCC occurred at τ = 0, which indicated that the unsteady aerodynamic load coefficients were obtained by the suggested strategies with no delay.

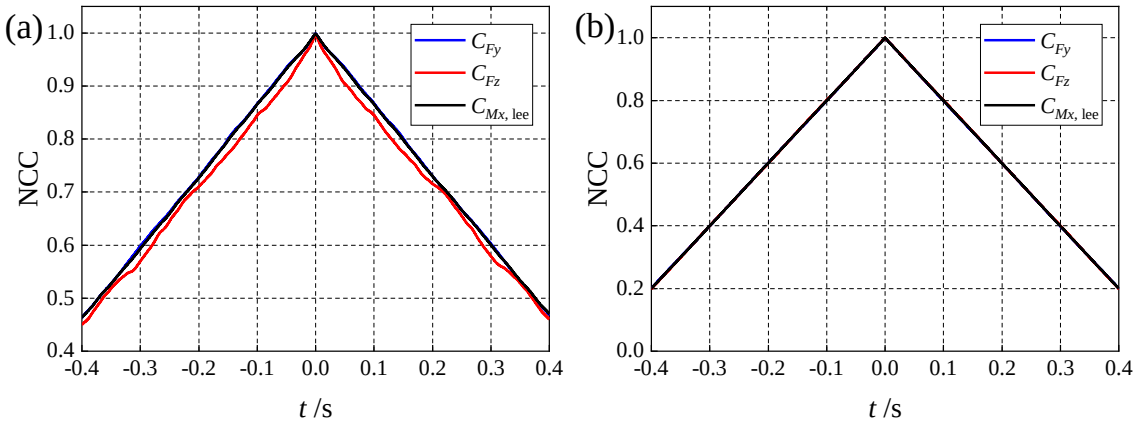

Fig. 21. Normalized cross-correlation of aerodynamic load coefficients: (a) BTV and (b) STV.

Fig. 22 illustrates the power spectral densities (PSDs) of the aerodynamic load coefficients of BTV and STV, where the blue and red lines are PSDs obtained by the discrete integration and numerical simulations, respectively, and the gray line is the ratio of the former to latter, i.e., the transfer function. PSDs are plotted against the Strouhal number (*St*), which is defined as

$$St = \frac{Hf}{v} \tag{13}$$

where *f* is the time-varying frequency of the aerodynamic load coefficients.

The fluctuations of the side force and rolling moment coefficients were similar [68,72], but the fluctuation of the lift coefficient was different from them. The cyan region in Fig. 22 represents the frequency range where the transfer function was less than 1.5, and PSDs obtained by the discrete integration could be considered similar to those obtained by the numerical simulations. This frequency range was approximately $St < 0.4$, the three aerodynamic load coefficients considered, and given that the side force most affected the running safety, as mentioned in Section 3.4. This was because almost all the large vortices near the vehicle were captured by the discrete integration, to which the low-frequency fluctuations were related. COOPER [73] found the break point of the aerodynamic admittance, and after calculations, it corresponded to *St* (based on the length of the vehicle) of 0.4. On the one hand, this confirmed the above view. On the other hand, the unsteady aerodynamic loads were proved to be accurate in this work. PSDs obtained by discrete integration were larger than those obtained by the numerical simulations at $St > 0.4$, indicating that the fluctuations of the aerodynamic load coefficients obtained by the discrete integration were large at high frequencies. These high-frequency fluctuations resulted from the separation and attachment of the small flow structures around the vehicles and the instability of the shear layers [5,7]. The high-frequency fluctuations might be captured by some taps and then be amplified by the discrete integration, as mentioned above.

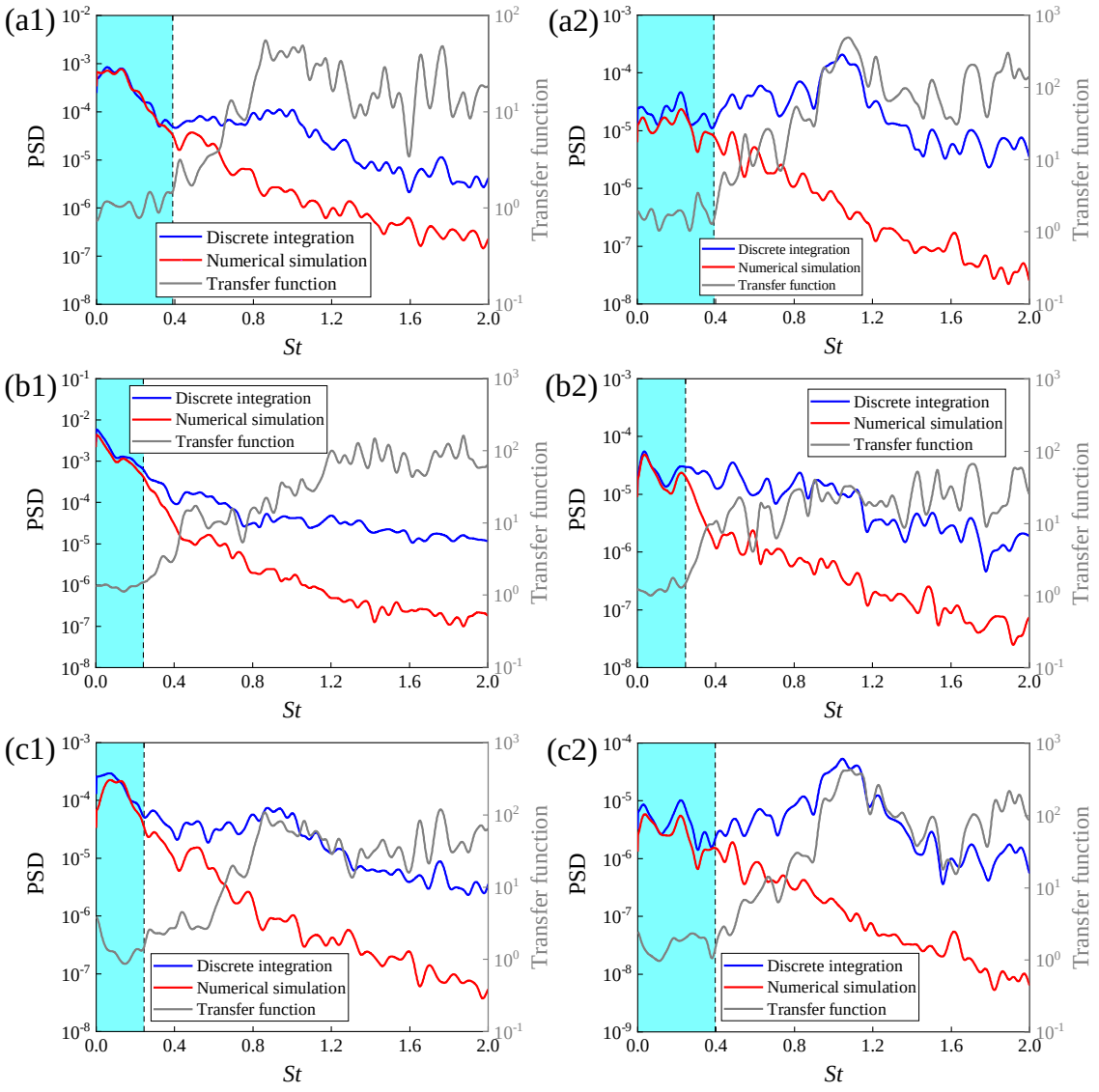

Fig. 22. Power spectrum densities of aerodynamic load coefficients: side force coefficients of (a1) BTV and (a2) STV, lift coefficients of (b1) BTV and (b2) STV, and rolling moment coefficients around lee rail of (c1) BTV and (c2) STV.

Fortunately, the results of the previous full-scale tests [18] and current numerical simulations illustrated that the most dominant frequencies of the aerodynamic load coefficients were at $St < 0.4$. Therefore, the suggested strategies could reflect the real frequency characteristics of the unsteady aerodynamic loads in the frequency range that people would be concerned about in crosswinds. The high-frequency fluctuations could be treated using an appropriate filter, which will become our research focus in the future.

The full-scale frequency corresponding to $St = 0.4$ was 4.938 Hz with the relative wind velocity of 50 m/s (the relatively large value measured in Gao et al. [18]). When the frequency of the pressure was less than 1 Hz, the error of the pressure was less than 5% with a plastic tubing (with an outer diameter of 2 mm and inner diameter of 1.8 mm) of which the length was

no more than 8 m, according to Liu et al. [20]. Therefore, the full-scale tests could be carried out using the suggested strategies and plastic tubing in combination.

4.5. Discussion on nonlinear interpolation

The interior of the above Lagrange rectangular element is linear, as mentioned in Section 4.1. This is not surprising: people expect nonlinear interpolation (NI) to improve the strategies, according to the mean pressure coefficients on the vehicle surfaces in Section 4.1 and Section 4.2. Fig. 23 illustrates the nonlinear interpolation of the mean pressure coefficients on the cross section X2−X2 of STV. The pressure taps at the midpoints of the elements are shown in Fig. 13(a), and the mean pressure coefficients on the cross section and taps are equal to those in Fig. 13(b) and (c). The modified Akima interpolation [74] was carried out, which modified the weights in the Akima algorithm for one-dimensional interpolation [75,76] and thus could avoid an overshoot. The Akima algorithm produces fewer undulations compared to the spline algorithm but is not as aggressively flattened compared to the pchip algorithm [74]. Different from the linear interpolation, the nonlinear one could basically reproduce the mean pressure coefficients on the vehicle surface, especially on the windward and leeward sides. But there is still gap with the goal of "close to the true value", which might have been due to the small amount of the taps.

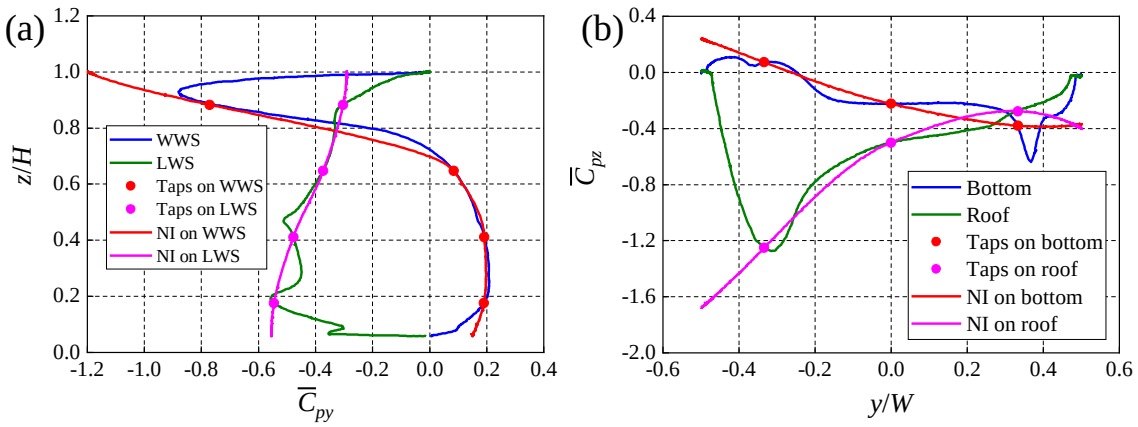

Fig. 23. Nonlinear interpolating among mean pressure coefficients at taps on: (a) WWS and LWS, as well as (b) bottom and roof of cross section X2−X2 of STV.

The mean aerodynamic force coefficients on the cross section X2−X2 of STV, including the side force and lift coefficients, could be obtained by adding up the nonlinear interpolation of the mean pressure coefficient. The mean aerodynamic force coefficients on the cross section X2−X2, meanwhile, could be calculated by the discrete integration reported in Section 2.1. Table 6 lists the errors of the aerodynamic force coefficients calculated by the means above (compared with the coefficients obtained by the numerical simulation), where the numbers in parentheses are absolute differences. The maximum error in the mean side force coefficient was

4.5%, while the one in the mean lift coefficient was 40.7% (the absolute difference was 0.044). The errors of the discrete integration and nonlinear interpolation were small and almost the same as each other. The error in the mean lift coefficient was slightly large, which might have been caused by the small number of the taps and the complex changes of the pressure on the bottom of the vehicle.

Table 6 Error of mean aerodynamic force coefficients on cross section X2−X2 of STV.

Algorithm	$\overline{C}_{Fy}$	$\overline{C}_{Fz}$
Discrete integration	4.2% (0.005)	28.9% (0.031)
Nonlinear interpolation	4.5% (0.005)	40.7% (0.044)

With the layout of the taps in Fig. 19, the accuracies of the aerodynamic load coefficients obtained by the discrete integration and nonlinear interpolation were similar. The error of the nonlinear interpolation was slightly large. The nonlinear interpolation could reproduce the continuously changed pressure, but it would need more taps than the discrete integration to improve the accuracy. There would be an optimal density of the taps in the nonlinear interpolation, which would be more complex than the layout in Fig. 19. This was opposite to the original intention of this work, which was to obtain the aerodynamic loads with the fewest number of the taps, rather than the continuously changed pressure on the surface. Therefore, the discrete integration was sufficient in the circumstances. In the future, the optimal density of the taps related to the nonlinear interpolation will be our research focus to reproduce the continuously changed pressure on the vehicle surface.

5. Conclusions

IDDES based on the SST k-ω turbulence model was carried out to calculate the aerodynamic loads and surface pressure on the bluff and streamlined vehicles. The discrete integration and discretization of the vehicle surfaces have been improved. The results are summarized as follows.

(1) The linearities of the surface pressure on the bluff and streamlined vehicles were generally high in the longitudinal, lateral, and vertical directions. The maximum R^2 in the elements was 0.9973. The vehicles could be discretized by the Lagrange rectangular elements. The linear of pressure on the streamlined vehicle body (excluding the streamlined head) was similar to that on the bluff vehicle.

(2) The strategy of the discretization based on the Lagrange rectangular elements was suggested to measure the aerodynamic loads on the vehicles in crosswinds. The discretization for all the vehicles was the same in the lateral and vertical directions, where the vehicles should be divided into at least three and four Lagrange rectangular elements, respectively. The

maximum vertical length should be 1000 mm. In the longitudinal direction, the bluff vehicle and streamlined vehicle body should be divided into at least five elements, whose largest length should be 4250 mm. The longitudinal length of the elements should be no more than 2700 mm on the streamlined head. If the locations of the taps were not available in tests, the taps would move around the midpoints of the longitudinal elements in the longitudinal direction, remaining the geometric features around the taps. The strategy required a relatively small amount of the taps, and the number of the taps on BTV and STV were 70 and 116, respectively. Note that the accuracy of the mean and unsteady aerodynamic loads would be uncontrollable and unpredictable if the discretization is not performed as required.

(3) The strategy of the discrete integration was suggested to measure the aerodynamic loads on the vehicles in crosswinds. The side force and lift were calculated with Eq. (1), and the rolling moment were determined by Eq. (2) and (3). The pressure should be projected into the directions of the aerodynamic forces to consider the real orientation of the elements. The difference of the projections of the pressure for calculating the lift could be obtained early by the numerical simulations, when using the differential piezoresistive transducers.

(4) The strategies of the discretization and discrete integration could be used to measure the mean aerodynamic loads accurately. The errors of the mean side force coefficient, lift, coefficient, and rolling moment coefficient around the lee rail of BTV were 2.5%, 12.9% and 4.1%, respectively, while the maximum error of STV was 2.2%. Compared with the previous studies, the strategies significantly improved the accuracy of the mean aerodynamic coefficients of STV, which was increased by up to 8.7%, while the accuracy of BTV was raised by 2.8%.

(5) The strategies suggested above could basically reproduced the unsteady aerodynamic loads. The fluctuation was larger than that in real situations. The amplitudes of the aerodynamic load coefficients increased by average 0.363, which was conservative. The unsteady aerodynamic loads with no delay were near to natural ones in the frequency range that people would be concerned about in crosswinds ($St < 0.4$).

(6) The suggested strategies were enough to be used in the full-scale tests with the plastic tubing. The differential piezoresistive transducers were suggested to be used in the full-scale tests. Additionally, the suggested strategies could be used in the model tests.

In the future, the suggested strategies will be used to measure the unsteady aerodynamic loads on the trains in natural crosswinds by the full-scale tests. The frequency characteristics of the aerodynamic loads obtained by the strategies and plastic tubing (see Liu et al. [20]) and the overestimation of the high-frequency fluctuations will be further studied. Moreover, the running safety (such as the relative wheel unloading) of the vehicles will be assessed based on the

strategies. The nonlinear interpolation and its layout of the taps will be studied deeply.

Acknowledgements

This work was supported by the Natural Science Foundation of Hunan Province, China (Grant numbers 2022JJ30727 and 2020JJ4737), the Science and Technology Innovation Program of Hunan Province, China (Grant No. 2022RC3040), the Technology Research and Development Program of China Railway Urumqi Group Co., Ltd. (Grant No. 2022-kj-70), China Scholarship Council (Grant No. 202206370140), and the Fundamental Research Funds for the Central Universities of Central South University (Grant No. 2022ZZTS0630). This work was carried out in part using computing resources at the High Performance Computing Center of Central South University.

References

[1] H.-q. Tian, Review of research on high-speed railway aerodynamics in China, Transportation Safety and Environment 1 (2019) 1–21. https://doi.org/10.1093/tse/tdz014.

[2] Z. Chen, T. Liu, W. Li, Z. Guo, Y. Xia, Aerodynamic performance and dynamic behaviors of a train passing through an elongated hillock region beside a windbreak under crosswinds and corresponding flow mitigation measures, Journal of Wind Engineering and Industrial Aerodynamics 208 (2021) 104434. https://doi.org/10.1016/j.jweia.2020.104434.

[3] B. Diedrichs, On computational fluid dynamics modelling of crosswind effects for high-speed rolling stock, Proceedings of the Institution of Mechanical Engineers, Part F: Journal of Rail and Rapid Transit 217 (2003) 203–226. https://doi.org/10.1243/095440903769012902.

[4] D. Flynn, H. Hemida, C. Baker, On the effect of crosswinds on the slipstream of a freight train and associated effects, Journal of Wind Engineering and Industrial Aerodynamics 156 (2016) 14–28. https://doi.org/10.1016/j.jweia.2016.07.001.

[5] Z. Guo, T. Liu, M. Yu, Z. Chen, W. Li, X. Huo, H. Liu, Numerical study for the aerodynamic performance of double unit train under crosswind, Journal of Wind Engineering and Industrial Aerodynamics 191 (2019) 203–214. https://doi.org/10.1016/j.jweia.2019.06.014.

[6] H. Hemida, C. Baker, Large-eddy simulation of the flow around a freight wagon subjected to a crosswind, Computers & Fluids 39 (2010) 1944–1956. https://doi.org/10.1016/j.compfluid.2010.06.026.

[7] H. Hemida, S. Krajnović, LES study of the influence of the nose shape and yaw angles on flow structures around trains, Journal of Wind Engineering and Industrial Aerodynamics

98 (2010) 34–46. https://doi.org/10.1016/j.jweia.2009.08.012.
[8] T.-H. Liu, J. Zhang, Effect of landform on aerodynamic performance of high-speed trains in cutting under cross wind, J. Cent. South Univ. 20 (2013) 830–836. https://doi.org/10.1007/s11771-013-1554-3.
[9] J. Zhang, G.-j. Gao, T.-H. Liu, Z.-w. Li, Crosswind stability of high-speed trains in special cuts, J. Cent. South Univ. 22 (2015) 2849–2856. https://doi.org/10.1007/s11771-015-2817-y.
[10] W. Khier, M. Breuer, F. Durst, Flow structure around trains under side wind conditions: a numerical study, Computers & Fluids 29 (2000) 179–195. https://doi.org/10.1016/S0045-7930(99)00008-0.
[11]C.J. Baker, M. Sterling, 2009. Aerodynamic Forces on Multiple Unit Trains in Cross Winds. Journal of Fluids Engineering 131, 101103. https://doi.org/10.1115/1.3222908.
[12] M. Bocciolone, F. Cheli, R. Corradi, S. Muggiasca, G. Tomasini, Crosswind action on rail vehicles: Wind tunnel experimental analyses, Journal of Wind Engineering and Industrial Aerodynamics 96 (2008) 584–610. https://doi.org/10.1016/j.jweia.2008.02.030.
[13] F. Cheli, F. Ripamonti, D. Rocchi, G. Tomasini, Aerodynamic behaviour investigation of the new EMUV250 train to cross wind, Journal of Wind Engineering and Industrial Aerodynamics 98 (2010) 189–201. https://doi.org/10.1016/j.jweia.2009.10.015.
[14] S. Giappino, D. Rocchi, P. Schito, G. Tomasini, Cross wind and rollover risk on lightweight railway vehicles, Journal of Wind Engineering and Industrial Aerodynamics 153 (2016) 106–112. https://doi.org/10.1016/j.jweia.2016.03.013.
[15] M. Suzuki, K. Tanemoto, T. Maeda, Aerodynamic characteristics of train/vehicles under cross winds, Journal of Wind Engineering and Industrial Aerodynamics 91 (2003) 209–218. https://doi.org/10.1016/S0167-6105(02)00346-X.
[16] C.J. Baker, J. Jones, F. Lopez-Calleja, J. Munday, Measurements of the cross wind forces on trains, Journal of Wind Engineering and Industrial Aerodynamics 92 (2004) 547–563. https://doi.org/10.1016/j.jweia.2004.03.002.
[17] M. Gallagher, J. Morden, C. Baker, D. Soper, A. Quinn, H. Hemida, M. Sterling, Trains in crosswinds – Comparison of full-scale on-train measurements, physical model tests and CFD calculations, Journal of Wind Engineering and Industrial Aerodynamics 175 (2018) 428–444. https://doi.org/10.1016/j.jweia.2018.03.002.
[18] H. Gao, T. Liu, H. Gu, Z. Jiang, X. Huo, Y. Xia, Z. Chen, Full-scale tests of unsteady aerodynamic loads and pressure distribution on fast trains in crosswinds, Measurement 186 (2021) 110152. https://doi.org/10.1016/j.measurement.2021.110152.
[19] K. Kikuchi, M. Suzuki, Study of aerodynamic coefficients used to estimate critical wind

speed for vehicle overturning, Journal of Wind Engineering and Industrial Aerodynamics 147 (2015) 1–17. https://doi.org/10.1016/j.jweia.2015.09.003.

[20] T.-H. Liu, L. Wang, Z.-W. Chen, H.-R. Gao, W.-H. Li, Z.-j. Guo, Y.-T. Xia, X.-S. Huo, Y.-W. Wang, Study on the pressure pipe length in train aerodynamic tests and its applications in crosswinds, Journal of Wind Engineering and Industrial Aerodynamics 220 (2022) 104880. https://doi.org/10.1016/j.jweia.2021.104880.

[21] C. Baker, The flow around high speed trains, Journal of Wind Engineering and Industrial Aerodynamics 98 (2010) 277–298. https://doi.org/10.1016/j.jweia.2009.11.002.

[22] X.-h. He, H. Li, Review of aerodynamics of high-speed train-bridge system in crosswinds, J. Cent. South Univ. 27 (2020) 1054–1073. https://doi.org/10.1007/s11771-020-4351-9.

[23] T. Liu, L. Wang, H. Gao, Y. Xia, Z. Guo, W. Li, H. Liu, 2022. Research progress on train operation safety in Xinjiang railway under wind environment. Transportation Safety and Environment 4, tdac005. https://doi.org/10.1093/tse/tdac005.

[24] S. Sanquer, C. Barré, M.D. de Virel, L.-M. Cléon, Effect of cross winds on high-speed trains: development of a new experimental methodology, Journal of Wind Engineering and Industrial Aerodynamics 92 (2004) 535–545. https://doi.org/10.1016/j.jweia.2004.03.004.

[25] F. Dorigatti, M. Sterling, C.J. Baker, A.D. Quinn, Crosswind effects on the stability of a model passenger train—A comparison of static and moving experiments, Journal of Wind Engineering and Industrial Aerodynamics 138 (2015) 36–51. https://doi.org/10.1016/j.jweia.2014.11.009.

[26] H. Gu, T. Liu, Z. Jiang, Z. Guo, Experimental and simulation research on the aerodynamic effect on a train with a wind barrier in different lengths, Journal of Wind Engineering and Industrial Aerodynamics 214 (2021) 104644. https://doi.org/10.1016/j.jweia.2021.104644.

[27] J. Niu, X. Liang, D. Zhou, Experimental study on the effect of Reynolds number on aerodynamic performance of high-speed train with and without yaw angle, Journal of Wind Engineering and Industrial Aerodynamics 157 (2016) 36–46. https://doi.org/10.1016/j.jweia.2016.08.007.

[28] X. Huo, T. Liu, M. Yu, Z. Chen, Z. Guo, W. Li, T. Wang, Impact of the trailing edge shape of a downstream dummy vehicle on train aerodynamics subjected to crosswind, Proceedings of the Institution of Mechanical Engineers, Part F: Journal of Rail and Rapid Transit 235 (2021) 201–214. https://doi.org/10.1177/0954409720915039.

[29] S. Loose, H. Richard, J. Bosbach, M. Thimm, W. Becker, M. Raffel, Optical measurement techniques for high Reynolds number train investigations, Exp Fluids 40 (2006) 643–653. https://doi.org/10.1007/s00348-005-0104-7.

[30] H. Gu, H. Gao, T. Liu, S. Cheng, J. Li, Z. Liu, Effects of windbreak wall model lengths on

aerodynamic characteristics of trains on different tracks in wind tunnel tests − a measurement strategy, Journal of Wind Engineering and Industrial Aerodynamics 228 (2022) 105104. https://doi.org/10.1016/j.jweia.2022.105104.

[31] F. Cheli, R. Corradi, D. Rocchi, G. Tomasini, E. Maestrini, Wind tunnel tests on train scale models to investigate the effect of infrastructure scenario, Journal of Wind Engineering and Industrial Aerodynamics 98 (2010) 353–362. https://doi.org/10.1016/j.jweia.2010.01.001.

[32] F. Cheli, S. Giappino, L. Rosa, G. Tomasini, M. Villani, Experimental study on the aerodynamic forces on railway vehicles in presence of turbulence, Journal of Wind Engineering and Industrial Aerodynamics 123 (2013) 311–316. https://doi.org/10.1016/j.jweia.2013.09.013.

[33] M. Schober, M. Weise, A. Orellano, P. Deeg, W. Wetzel, Wind tunnel investigation of an ICE 3 endcar on three standard ground scenarios, Journal of Wind Engineering and Industrial Aerodynamics 98 (2010) 345–352. https://doi.org/10.1016/j.jweia.2009.12.004.

[34] C. Sicot, F. Deliancourt, J. Boree, S. Aguinaga, J.P. Bouchet, Representativeness of geometrical details during wind tunnel tests. Application to train aerodynamics in crosswind conditions, Journal of Wind Engineering and Industrial Aerodynamics 177 (2018) 186–196. https://doi.org/10.1016/j.jweia.2018.01.040.

[35] G. Tomasini, S. Giappino, F. Cheli, P. Schito, Windbreaks for railway lines: Wind tunnel experimental tests, Proceedings of the Institution of Mechanical Engineers, Part F: Journal of Rail and Rapid Transit 230 (2016) 1270–1282. https://doi.org/10.1177/0954409715596191.

[36] E. Brambilla, S. Giappino, G. Tomasini, Wind tunnel tests on railway vehicles in the presence of windbreaks: Influence of flow and geometric parameters on aerodynamic coefficients, Journal of Wind Engineering and Industrial Aerodynamics 220 (2022) 104838. https://doi.org/10.1016/j.jweia.2021.104838.

[37] H. Gu, T. Liu, Z. Jiang, Z. Guo, Research on the wind-sheltering performance of different forms of corrugated wind barriers on railway bridges, Journal of Wind Engineering and Industrial Aerodynamics 201 (2020) 104166. https://doi.org/10.1016/j.jweia.2020.104166.

[38] H. Gu, T. Liu, H. Gao, Z. Liu, S. Cheng, Wind tunnel testing on the aerodynamic effect on a train with single-sided and double-sided wind barriers of different lengths, Proceedings of the Institution of Mechanical Engineers, Part F: Journal of Rail and Rapid Transit (2022) 095440972211165. https://doi.org/10.1177/09544097221116551.

[39] Y. Noguchi, M. Suzuki, C. Baker, K. Nakade, Numerical and experimental study on the aerodynamic force coefficients of railway vehicles on an embankment in crosswind,

Journal of Wind Engineering and Industrial Aerodynamics 184 (2019) 90–105. https://doi.org/10.1016/j.jweia.2018.11.019.

[40] G. Tomasini, S. Giappino, R. Corradi, Experimental investigation of the effects of embankment scenario on railway vehicle aerodynamic coefficients, Journal of Wind Engineering and Industrial Aerodynamics 131 (2014) 59–71. https://doi.org/10.1016/j.jweia.2014.05.004.

[41] L. Zhang, M.-z. Yang, X.-f. Liang, Experimental study on the effect of wind angles on pressure distribution of train streamlined zone and train aerodynamic forces, Journal of Wind Engineering and Industrial Aerodynamics 174 (2018) 330–343. https://doi.org/10.1016/j.jweia.2018.01.024.

[42] S. Avila-Sanchez, S. Pindado, O. Lopez-Garcia, A. Sanz-Andres, Wind tunnel analysis of the aerodynamic loads on rolling stock over railway embankments: the effect of shelter windbreaks, ScientificWorldJournal. 2014 (2014) 421829. https://doi.org/10.1155/2014/421829.

[43] S.A. Hashmi, H. Hemida, D. Soper, Wind tunnel testing on a train model subjected to crosswinds with different windbreak walls, Journal of Wind Engineering and Industrial Aerodynamics 195 (2019) 104013. https://doi.org/10.1016/j.jweia.2019.104013.

[44] X.-h. He, T.-h. Zuo, Y.-f. Zou, L. Yan, L.-b. Tang, Experimental study on aerodynamic characteristics of a high-speed train on viaducts in turbulent crosswinds, J. Cent. South Univ. 27 (2020) 2465–2478. https://doi.org/10.1007/s11771-020-4462-3.

[45] C.J. Baker, The wind tunnel determination of crosswind forces and moments on a high speed train, in: E.H. Hirschel, K. Fujii, W. Haase, B. Leer, M.A. Leschziner, M. Pandolfi, J. Periaux, A. Rizzi, B. Roux, B. Schulte-Werning, R. Grégoire, A. Malfatti, G. Matschke (Eds.), TRANSAERO — A European Initiative on Transient Aerodynamics for Railway System Optimisation, Springer Berlin Heidelberg, Berlin, Heidelberg, 2002, pp. 46–60.

[46] R.K. COOPER, THE PROBABILITY OF TRAINS OVERTURNING IN HIGH WINDS, in: Wind Engineering, Elsevier, 1980, pp. 1185–1194.

[47] D. Soper, C. Baker, M. Sterling, An experimental investigation to assess the influence of container loading configuration on the effects of a crosswind on a container freight train, Journal of Wind Engineering and Industrial Aerodynamics 145 (2015) 304–317. https://doi.org/10.1016/j.jweia.2015.03.002.

[48] T. Liu, Z. Chen, Z. Guo, S. Krajnović, Reasonable pressure tap layout to measure the aerodynamic forces of a train at different yaw angles, Measurement 166 (2020) 108255. https://doi.org/10.1016/j.measurement.2020.108255.

[49] X.-h. Xiong, X.-f. Liang, G.-j. Gao, T.-H. Liu, Train aerodynamic characteristics in strong

cross-wind on Lanzhou-Xinjiang railway line, Journal of Central South University (Science and Technology) 37 (2006) 1183–1188.

[50] CEN European Standard, Railway applications - Aerodynamics. Part 1: Symbols and units, EN 14067-1, 2003.

[51] G.-j. Gao, L.-l. Duan, X.-j. Miao, Overturning stability of box-car on Qinghai-Tibet railway line with strong cross wind, Journal of Central South University (Science and Technology) 42 (2011) 1150–1155.

[52] CEN European Standard, Railway applications - Aerodynamics. Part 6: Requirements and test procedures for cross wind assessment, EN 14067-6, 2022.

[53] M.L. Shur, P.R. Spalart, M.K. Strelets, A.K. Travin, A hybrid RANS-LES approach with delayed-DES and wall-modelled LES capabilities, International Journal of Heat and Fluid Flow 29 (2008) 1638–1649. https://doi.org/10.1016/j.ijheatfluidflow.2008.07.001.

[54] T. Li, D. Qin, J. Zhang, Effect of RANS Turbulence Model on Aerodynamic Behavior of Trains in Crosswind, Chin. J. Mech. Eng. 32 (2019) 103. https://doi.org/10.1186/s10033-019-0402-2.

[55] SIEMENS, STAR-CCM+ Documentation: Version 13.02, 2018.

[56] J.A. Morden, H. Hemida, C.J. Baker, 2015. Comparison of RANS and Detached Eddy Simulation Results to Wind-Tunnel Data for the Surface Pressures Upon a Class 43 High-Speed Train. Journal of Fluids Engineering 137, 041108. https://doi.org/10.1115/1.4029261.

[57] J. Niu, D. Zhou, Y. Wang, Numerical comparison of aerodynamic performance of stationary and moving trains with or without windbreak wall under crosswind, Journal of Wind Engineering and Industrial Aerodynamics 182 (2018) 1–15. https://doi.org/10.1016/j.jweia.2018.09.011.

[58] Z. Guo, T. Liu, Z. Liu, X. Chen, W. Li, An IDDES study on a train suffering a crosswind with angles of attack on a bridge, Journal of Wind Engineering and Industrial Aerodynamics 217 (2021) 104735. https://doi.org/10.1016/j.jweia.2021.104735.

[59] X.-S. Huo, T.-H. Liu, Z.-W. Chen, W.-H. Li, J.-Q. Niu, H.-R. Gao, Aerodynamic characteristics of double-connected train groups composed of different kinds of high-speed trains under crosswinds: A comparison study, Alexandria Engineering Journal (2022). https://doi.org/10.1016/j.aej.2022.09.011.

[60] W. Li, T. Liu, P. Martinez-Vazquez, Z. Guo, X. Huo, Y. Xia, Z. Chen, Effects of embankment layouts on train aerodynamics in a wind tunnel configuration, Journal of Wind Engineering and Industrial Aerodynamics 220 (2022) 104830. https://doi.org/10.1016/j.jweia.2021.104830.

[61] Y. Xia, T. Liu, W. Li, X. Dong, Z. Chen, Z. Guo, Numerical comparisons of the aerodynamic performances of wind-tunnel train models with different inter-carriage gap spacings under crosswind, Journal of Wind Engineering and Industrial Aerodynamics 214 (2021) 104680. https://doi.org/10.1016/j.jweia.2021.104680.

[62] J. Zhang, K. He, J. Wang, T. Liu, X. Liang, G. Gao, Numerical Simulation of Flow around a High-Speed Train Subjected to Different Windbreak Walls and Yaw Angles, JAFM 12 (2019) 1137–1149. https://doi.org/10.29252/jafm.12.04.29484.

[63] W. Li, T. Liu, P. Martinez-Vazquez, Z. Chen, X. Huo, D. Liu, Y. Xia, Correlation tests on train aerodynamics between multiple wind tunnels, Journal of Wind Engineering and Industrial Aerodynamics 229 (2022) 105137. https://doi.org/10.1016/j.jweia.2022.105137.

[64] R. Killick, P. Fearnhead, I.A. Eckley, Optimal Detection of Changepoints With a Linear Computational Cost, Journal of the American Statistical Association 107 (2012) 1590–1598. https://doi.org/10.1080/01621459.2012.737745.

[65] M. Lavielle, Using penalized contrasts for the change-point problem, Signal Processing 85 (2005) 1501–1510. https://doi.org/10.1016/j.sigpro.2005.01.012.

[66] MathWorks, Signal Processing Toolbox document, 2022.

[67] Z. Guo, T. Liu, Z. Chen, Z. Liu, A. Monzer, J. Sheridan, Study of the flow around railway embankment of different heights with and without trains, Journal of Wind Engineering and Industrial Aerodynamics 202 (2020) 104203. https://doi.org/10.1016/j.jweia.2020.104203.

[68] J. Zhang, K. He, X. Xiong, J. Wang, G. Gao, Numerical Simulation with a DES Approach for a High-Speed Train Subjected to the Crosswind, JAFM 10 (2017) 1329–1342. https://doi.org/10.18869/acadpub.jafm.73.242.27566.

[69] Z. Jiang, T. Liu, H. Gu, Z. Guo, A numerical study of aerodynamic characteristics of a high-speed train with different rail models under crosswind, Proceedings of the Institution of Mechanical Engineers, Part F: Journal of Rail and Rapid Transit 235 (2021) 840–853. https://doi.org/10.1177/0954409720969250.

[70] Z. Guo, T. Liu, Y. Xia, Z. Liu, Aerodynamic influence of the clearance under the cowcatcher of a high-speed train, Journal of Wind Engineering and Industrial Aerodynamics 220 (2022) 104844. https://doi.org/10.1016/j.jweia.2021.104844.

[71] D. Liu, T. Wang, X. Liang, S. Meng, M. Zhong, Z. Lu, High-speed train overturning safety under varying wind speed conditions, Journal of Wind Engineering and Industrial Aerodynamics 198 (2020) 104111. https://doi.org/10.1016/j.jweia.2020.104111.

[72] M. Yu, R. Jiang, Q. Zhang, J. Zhang, Crosswind Stability Evaluation of High-Speed Train Using Different Wind Models, Chin. J. Mech. Eng. 32 (2019). https://doi.org/10.1186/s10033-019-0353-7.

[73] R.K. COOPER, Atmospheric turbulence with respect to moving ground vehicles, Journal of Wind Engineering and Industrial Aerodynamics 17 (1984) 215–238. https://doi.org/10.1016/0167-6105(84)90057-6.
[74] MathWorks, MATLAB Mathematics, 2022.
[75] H. Akima, A method of bivariate interpolation and smooth surface fitting based on local procedures, Commun. ACM 17 (1974) 18–20. https://doi.org/10.1145/360767.360779.
[76] H. Akima, A New Method of Interpolation and Smooth Curve Fitting Based on Local Procedures, J. ACM 17 (1970) 589–602. https://doi.org/10.1145/321607.321609.